Laser control and electron dynamics of ultrafast energy transfer processes in quantum dots

Inaugural-Dissertation

to obtain the academic degree

Doctor rerum naturalium (Dr. rer. nat.)

submitted to the Department of Biology, Chemistry and Pharmacy

of Freie Universität Berlin

by

ANIKA HALLER

from Berlin

2019

This work was prepared under supervision of

Dr. Annika Bande (Helmholtz-Zentrum Berlin)

between June 2015 and June 2019.

1. Referee:	Dr. Annika Bande
2. Referee:	Prof. Dr. Beate Paulus

Date of defense: September 3rd, 2019

Abstract

The inter-Coulombic decay (ICD) is an ultrafast energy transfer process between an electronically excited species that relaxes and a neighboring one that is simultaneously ionized. This Coulomb interaction mediated mechanism has been recently discovered likewise in atomic, molecular, biological, and nanostructured systems, whereas the latter ones require more sophisticated theoretical interpretations as well as an experimental proof.

In this thesis, ICD is theoretically studied focusing on the role of the efficient decay of a two-electron resonance excited state in a pair of negatively charged quantum dots (QD). The outcome is an electron in the continuum and the second one in the ground level of the formerly excited QD. To this end, electron dynamics calculations are performed with the antisymmetrized multiconfiguration time-dependent Hartree method.

The initiation and control of ICD are carried out by means of a resonant infrared laser pulse of picosecond length. The process is optimized by studying competing excitation processes under a variation of the focus and the intensity of the exciting laser. Those competing processes are direct ionizations and multi-photon excitations, which prevent the QDs from undergoing ICD and shall therefore be avoided. Moreover, the impact of the laser polarization on the electron emission direction is studied.

Two types of QDs are examined. In the first type the QDs are embedded inside a nanowire, such that emitted electrons can only move along a single continuum direction. For reasons of experimental feasibility and in view of potential device applications, the second type of QD conformation is considered, which is generally more widely investigated. In this case, the QDs are arranged on a two-dimensional wetting layer and the electrons can escape from the dots into the continuous surface.

Consequently, the highest ICD efficiency is achieved for excitations by resonant π-pulses. Moreover, the laser should be focused on the specific dot that shall be brought to an excited level as part of the resonance state. Additional efficiency gain is obtained when allowing for a two-dimensional continuum as in laterally arranged dots. For these QDs the laser polarization has an impact on the decaying state, which is a mixture of resonance states of both directions.

The QD-ICD in the presented systems is an efficient and promising process for future QD infrared photodetectors. This is due to its sensitivity to weak and low-frequency light. Besides, the energy conversion into an electric current is enhanced through the intermediate ICD process, in comparison to already existing devices that function via direct QD ionization.

Kurzzusammenfassung

Der inter-Coulomb-Zerfall (aus dem Englischen auch kurz ICD genannt) ist ein ultraschneller Energietransferprozess zwischen einem elektronisch angeregten Partner, welcher relaxiert, und einem Nachbarn, der infolgedessen ionisiert wird. Dieser durch Coulombwechselwirkung herbeigeführte Mechanismus wurde kürzlich entdeckt und gilt in Atomen, Molekülen, biologischen System und Nanostrukturen. Letztere benötigen im Vergleich zu den anderen Systemen noch mehr ausgereifte theoretische Interpretationen sowie einen experimentellen Nachweis.

Diese Doktorarbeit befasst sich mit der Theorie um ICD, wobei der effiziente Zerfall eines resonant angeregten zwei-Elektronen Zustands in einem Paar einfach negativ geladener Quantenpunkte (QP) betrachtet wird. Am Ende befindet sich ein Elektron im energetischen Kontinuum und das andere im Grundlevel des zuerst angeregten QPs. Die Berechnungen der Elektronendynamik werden mithilfe der antisymmetrierten "multiconfiguration time-dependent Hartree" (MCTDH) Methode durchgeführt.

Die Anregung und Kontrolle des ICD Prozesses werden mittels resonanter Laserpulse realisiert, welche energetisch im infraroten Bereich des Spektrums und zeitlich bei ein paar Picosekunden liegen. Zur Optimierung von ICD werden konkurrierende Prozesse unter variierendem Fokus und Intensität des anregenden Lasers untersucht. Dabei handelt es sich um direkte Ionisationen oder Multiphotonen-Angregungen, welche verhindern dass ICD in den QP stattfinden kann und deshalb möglichst vermieden werden sollen. Daneben wird auch der Einfluss der Laserpolarisation auf die Elektronenemissionsrichtung untersucht.

Es werden hier zwei verschiedene Arten von QP betrachtet. Zum einen befindet sich das QP-Paar in einem Nanodraht, sodass sich emittierte Elektronen nur entlang einer Kontinuumsdimension bewegen können. Aus Gründen der experimentellen Durchführbarkeit und mit Blick auf potentielle Anwendung für elektronische Bauelemente, wird noch eine zweite Art von QP-Formation betrachtet, welche auch generell mehr erforscht ist. In diesem Fall sind die QP auf einer zweidimensionalen Benetzungsschicht angeordnet. Folglich kann sich das ICD-Elektron in zwei Raumrichtungen bewegen.

Es kann gezeigt werden, dass ICD besonders effizient nach der Anregung mit einem resonanten π-Puls ist. Des weiteren sollte der Laser nur auf denjenigen QP fokussiert werden, welcher das angeregte Elektron des Zerfallszustands tragen soll. Daneben kann die Effizienz erhöht werden, wenn sich das ICD-Elektron in zwei Kontinuumsdimensionen bewegen kann. In diesem Fall haben auch verschiedene Laserpolarisationen einen Einfluss auf den Zerfallszustand, welcher sich aus den Resonanzzuständen beider Dimensionen zusammensetzt.

Der QP-ICD Prozess ist für beide Systeme, die hier präsentiert werden, ein effizienter und vielversprechender Mechanismus für zukünftige QP Infrarotdetektoren. Dies kommt durch seine Sensitivität für schwaches und niederfrequentes Licht. Daneben ist durch ICD, als Zwischenschritt der Lichtabsorption, die Energieumwandlung in elektrischen Strom verbessert im Vergleich zu existierenden Detektoren, welche durch direkte Ionisation des QPs funktionieren.

Danksagung

An dieser Stelle möchte ich mich bei allen Menschen bedanken, die diese Arbeit durch ihre Unterstützung ermöglicht haben.

Allen voran danke ich meiner Betreuerin Annika Bande dafür, dass sie in meine Fähigkeiten vertraut und mich als ihre erste Doktorandin gewählt hat. Durch ihre geduldige und verständnisvolle Art habe ich mich stets rundum gut betreut gefühlt. Dabei hat sie sich immer wieder die Zeit genommen, mir den richtigen Weg zu weisen. Vielen Dank für die Möglichkeit eines Forschungsaufenthalts in Lille, sowie auch für spannende Konferenzreisen. Ich werde immer mit Freude auf den Noraebang-Abend in Südkorea zurückblicken und den DPG Talk im Pathologiehörsaal in Erlangen als kuriose Erfahrung in Erinnerung behalten. Ich hoffe, irgendwann einmal Quantenpunkt-ICD als Anwendung im alltäglichen Leben begegnen zu können.

Außerdem möchte ich mich ganz herzlich bei Beate Paulus für die Übernahme der Rolle als Zweitgutachterin bedanken, sowie für die Einladung zu diversen Vorträgen in das Seminar an der FU.

Vielen Dank an die ganze AG-Bande am HZB für die gemeinsame Zeit. Das sind Fabian Weber, Axel Molle, Matthias Berg, Pascal Krause und alle weiteren und ehemaligen Mitglieder. Vielen Dank auch an Christoph Merschjann dafür, dass er mich in sein goldenes Büro einziehen ließ.

Mein Dank gilt auch Daniel Peláez für die großartige Zusammenarbeit, aus der mein letztes Paper hervorgegangen ist, sowie für die freundliche Aufnahme in Lille für einen zweiwöchigen Forschungsaufenthalt.

Ein besonderer Dank geht an meine gesamte Familie für die bedingungslose Unterstützung und den Zusammenhalt in jeder Lebenslage. Ohne meine Eltern hätte ich es nicht so weit geschafft.

I would like to thank Won Kyu Kim for his support and believing in me all the time.
김원규 감사합니다.

Ein letzter Dank soll an meinen Physik- und Mathelehrer Herrn Göhlert gerichtet sein. Sein Unterricht hat mich für die Physik begeistert.

Contents

List of Publications

Paper A1 Anika Haller, Ying-Chih Chiang, Maximilian Menger, Emad F. Aziz and Annika Bande
"Strong field control of the interatomic Coulombic decay process in quantum dots"
Chem. Phys., **482**:135-145, 2017
DOI: 10.1016/j.chemphys.2016.09.020
URL: https://doi.org/10.1016/j.chemphys.2016.09.020

Paper A2 Anika Haller and Annika Bande
"Favoritism of quantum dot inter-Coulombic decay over direct and
multi-photon ionization by laser strength and focus"
J. Chem. Phys., **149**:134102, 2018
DOI: 10.1063/1.5042208
URL: https://doi.org/10.1063/1.5042208

Paper A3 Anika Haller, Daniel Peláez and Annika Bande
"Inter-Coulombic decay in laterally arranged quantum dots controlled by polarized lasers"
J. Phys. Chem. C, **123**:14754-14765, 2019
DOI: 10.1021/acs.jpcc.9b01250
URL: https://doi.org/10.1021/acs.jpcc.9b01250

1 Introduction

Nowadays, the biggest quantum leaps in research are achieved through interdisciplinary work, combining expertise from different fields of science. This theoretical thesis presents a connection of the laser control of ultrafast energy transfer processes with nano-sized solid state systems and with electron dynamics calculations.

Before talking about dynamics it is useful to take a look at static chemical and physical systems as treated by quantum chemistry. As a long-established field of theoretical sciences, quantum chemistry aims at describing the distribution of electrons within the orbitals, i.e., the discrete levels, of an atomic or molecular system to conclude on its chemical properties. The electron configuration of lowest total energy represents the system's *ground state*, in which orbitals are filled with electrons from the lowest to the highest potential energy without leaving a *hole*, i.e., an electron vacancy. The dynamical aspect comes into play, for example, in an excitation process that brings the system from the ground state into an *excited state*, thus a state of energy above the ground state. This process requires energy, for example, in form of a photon that is absorbed by an electron inside an atom or molecule. For *resonant* excitations the potential energy of the electron is lifted by the photon energy $\hbar\omega$ and the electron resides consequently in a higher orbital. Otherwise, for large enough excitation energies the electron may even be removed completely in a *photoionization* process, leaving a positively charged atom or molecule. The inverse process in which energy is released is the *decay* from an excited state into a state of lower energy that can be above or equal to the ground state energy and either bound or ionized. There exists a variety of decay mechanisms. The relative importance of a certain decay process depends on the presence of competing processes as well as on their relative efficiencies.

In principle, the decay of an isolated excited atom or molecule takes place *locally*, that means within the same atom or molecule, as shown in Fig. 1 (a) and (b). On the one hand, the decay can occur spontaneously by emission of radiation (photon decay) or via vibrational relaxation (phonon decay), as presented in (a). Those decaying states are long-lived and of low energy. In comparison, high-energetic excited states are of much shorter lifetime and can decay by an intra-atomic or -molecular autoionization mechanism known as the *Auger process*,[1] as shown in (b). There, an electron of high potential, i.e., from an outer orbital, drops into an inner hole state of low potential energy. The excess energy is transferred to another electron within the same atom or molecule. The energy receiving electron is brought into a state above the ionization threshold, thus having non-zero kinetic energy to escape the system, which is left doubly ionized. Otherwise, in atoms very deep inner-shell excitations may also decay by emission of high-energetic X-rays.[2]

For low-energetic excited states with a hole in an outer orbital the Auger decay is energetically forbidden, leaving seemingly radiative and vibrational decay as only options. However, the decay processes were found to look very different within clusters of atoms or molecules with only weak chemical bonding between the individual monomers, as *non-local* processes tend to play a major role here. It has been found that inner-valence excited atoms are likely to decay by non-radiative

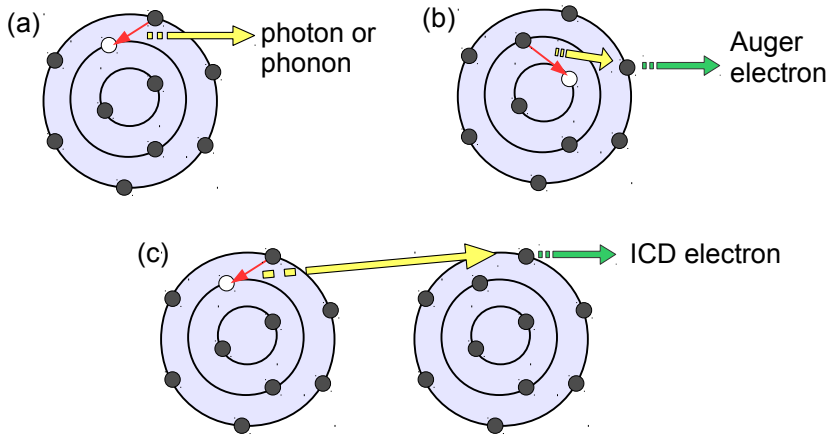

Figure 1: Comparison of different decay mechanisms in atomic systems. (a) An isolated atom with an inner-valence excited state can decay by emission of a photon or a phonon. (b) For a core excited state the atom can decay by electron emission via the Auger process. (c) Otherwise, an atom with an inner-valence excited state may decay non-locally via ICD if another atom is present.

energy transfer processes if at least one neighboring atom or molecule is present. One type of such a non-local and non-radiative process is the Förster resonance energy transfer (FRET),[3] which is mostly described for biological systems, i.e., uncoupled and loosely bound molecule complexes.[4] Here, one site de-excites by transferring energy to a neighbor, which is in consequence resonantly excited, however not ionized. This energy transfer process is explained by the dipole-dipole coupling between the two sites, that means the electrostatic interaction between neighbors with permanent dipole. In general, FRET can also be formulated for non-biological systems, as has been done for example for nanostructures.[5]

In the sense of non-radiative energy transfer in clusters, another more ubiquitous non-local decay mechanism of an inner-valence excitation was proposed by Cederbaum et al.[6] More precisely, it is an autoionization process mediated by long-range Coulomb interactions between electrons placed at different atomic or molecular sites. It is called the *interatomic* or *intermolecular Coulombic decay*, or short ICD, cf. Fig. 1 (c). This terminology has been introduced by Zobeley et al.[7] However, one may also use the term *inter-Coulombic decay*, which accounts for the generality of the process with respect to the system type. In detail, ICD is explained as follows: an outer-valence electron drops into the inner-valence vacancy and the excess energy is transferred to an outer-valence electron in a neighboring atom or molecule which in consequence is ionized. The ejected *ICD electron* is of relatively low energy, i.e., a few eV, in comparison to several 100 eV for a typical Auger electron.[8] The result is a doubly outer-valence ionized cluster. In weakly bound systems this can lead to repulsion between two positively charged monomers and hence to fragmentation of the system, also known as *Coulomb explosion*.[6], [9] In comparison to the lifetimes of the radiatively decaying states in small atomic clusters (≈ picoseconds),[10] ICD is ultrafast with femtosecond decay times, which makes it the dominant relaxation pathway. Furthermore,

other than for FRET the energy transfer in ICD takes place non-resonantly as the electronic final state is unbound. Therefore, ICD is a more general process and possible in a large variety of systems,[10]–[13] as will be elaborated further below.

Mathematically, the matrix element

$$\langle \mathrm{iv}, \varepsilon | \hat{V}_{\mathrm{Coul}} | \mathrm{ov}, \mathrm{ov}' \rangle = \iint \mathrm{d}\mathbf{r}_1 \mathrm{d}\mathbf{r}_2 \, \psi^*_{\mathrm{iv},\varepsilon}(\mathbf{r}_1, \mathbf{r}_2) \, \frac{1}{|\mathbf{r}_1 - \mathbf{r}_2|} \, \psi_{\mathrm{ov},\mathrm{ov}'}(\mathbf{r}_1, \mathbf{r}_2) \tag{1}$$

describes the two-site transition process mediated by the Coulomb interaction $\hat{V}_{\mathrm{Coul}}$ between two electrons with spatial coordinates $\mathbf{r}_1$ and $\mathbf{r}_2$. There, one outer-valence (ov) electron drops into the inner-valence (iv) vacancy and another outer-valence electron (ov') is ejected into a continuum state with kinetic energy ε.[6] Even without overlap the two orbitals $|\mathrm{ov}\rangle$ and $|\mathrm{ov}'\rangle$ are efficiently connected by the low energetic electron of large wavelength ejected from $|\mathrm{ov}'\rangle$.[11],[14] The matrix element Eq. (1) factorizes into a *direct* and an *exchange* term, which is due to the indistinguishability of electrons. More precisely, the ov electron either drops into the iv vacancy within the same atom (direct) or the neighbor atom (exchange). For the latter this would mean that instead of energy an electron is transferred, which is known as *electron transfer mediated decay*.[11],[15],[16] It was found that mainly direct contributions, i.e., decay by energy transfer, determine ICD as the ov orbitals of the neighboring atoms or molecules overlap only little.[14] Some researchers also use the picture of a virtual photon to describe the energy exchange in ICD.[14] In general, ICD after resonant excitation is called resonance ICD (RICD).[17],[18] If the excited iv electron also de-excites into the iv hole, the process is called participator RICD (pRICD).[19] The iv hole may also be filled with an ov electron in spectator RICD (sRICD).[20] Besides, ICD is also possible via transfer of vibrational energy for vibrationally excited molecules that are in their electronic ground state.[21]

In the last three decades there have been many observations of ICD and ICD-like processes theoretically and experimentally in various systems, which have already been collected in several reviews from theoretical[11],[12] and experimental view point.[10],[13] The very first theoretical predictions were made for small hydrogen bonded systems like HF compounds and water molecules.[6],[7],[22],[23] The continuously ongoing theoretical investigations of ICD have led to the study of the neon dimer as prototype of van-der-Waals bonded systems in which ICD takes place.[24]–[26] A first experimental proof of ICD was found by analyzing the photon excited electron spectra of large Ne clusters of average 70 atoms.[27] Follow-up experimental observation of ICD have been made in inner-valence ionized Ne dimers.[9],[28]

The ICD decay rate, as inverse of the lifetime, increases with the number of open channels and so does the efficiency of ICD. For example, the decaying electronic state of Ne_2^+ supports 11 discrete vibrational autoionizing states that are each decaying by ICD with their specific lifetime adding to the rate.[24] From the first years of study, some conclusions on ICD intensified. Firstly, the number of decay channels and thus the efficiency of ICD increases with number of neighbors. In this regard, it was found for free Ne clusters that the ICD lifetime of a 2s vacancy at a surface site is larger (> 30 fs) than in bulk atoms (< 10 fs).[28] Secondly, the ICD lifetime is extremely

sensitive to internuclear distances. For growing distances between the atoms ICD is suppressed, as the Coulomb interactions reduce.[26] Thirdly, the ICD rate shows $\propto R^{-6}$ behavior like for the dipole-dipole coupled decay as in FRET, but becomes much faster when overlapping sets in for atoms or molecules approaching each other.[14], [29] That is however only up to a minimal distance, as ICD is suppressed if monomers get too close.[6]

That "ICD appears everywhere"[30] becomes obvious when looking at the over two hundred publications that have described ICD or ICD-like processes as very common phenomena occurring in many kinds of weakly bound systems. ICD was found for example in a cascade after an Auger decay,[31]–[33] or within solutions[34], [35] and water clusters.[36], [37] ICD may further occur after electron capture,[38]–[41] after collision with high-energetic ions[42], [43] or electrons,[44], [45] or even as a process in the repair of UV-radiation damaged DNA.[46], [47]

So far, ICD was presented to occur especially in atomic and molecular clusters. In this thesis it shall be treated within systems of nano-sized semiconductors named *quantum dots* (QD),[48]–[51] where ICD was predicted recently.[52]–[54] QD structures are solid state material usually assembled by a few thousand atoms. Their name reveals a three-dimensional spatial confinement ("dot") that leads to a discretization in electronic energies ("quantum"). Obviously, QDs are of much different scales than atoms or molecules, yet it was found that the same principles hold, as actually QDs can be considered as "artificial atoms".[55] In fact, radiative[56] and Auger decay[57]–[60] have already been observed for QDs, thus researchers suggested that ICD should also work for systems of at least two spatially separated QDs for which Auger decay is forbidden.[52], [53]

The process has been first suggested in QD dimers by a theoretical approach of Cherkes et al.[52] In their theoretical model a confining potential of two three-dimensional negative Gaussian potentials represents a pair of non-coupled spherically shaped QDs made of GaAs. The resonantly excited state of the two singly negatively charged QDs, separated by a distance of 10 nm, was found to decay via ICD within a few ps. In detail, within the conduction band an excited electron decays to a lower level within the same QD by simultaneously transferring its energy to the electron in the other dot, which in consequence is ionized.

The QD-ICD idea was picked up by researchers from Heidelberg.[53], [54], [61], [62] Their studies build the fundament to which this thesis is tied. Bande et al.[53] used time-dependent calculation methods for studying the electron dynamics of ICD in a QD pair in real time. Similar to the QD potential described above, the dots are here represented by two finite wells in form of negative Gaussian potentials, however only within the aligning z direction. The motion in the transversal directions (x, y) is strongly confined by infinite parabolic potentials, in which the electrons are strongly tied to their equilibrium ground state position. In consequence, the electrons are very unlikely to be excited to a higher level in x and y, at least not for the energies appearing here. This gives an overall simplified effective *quasi one-dimensional* system. The potential parameters are chosen such that the two QDs are well separated, and the "left" dot supports two levels (L_0, L_1) and the "right" one a single level (R_0), cf. Fig. 2. For this system ICD looks as follows:

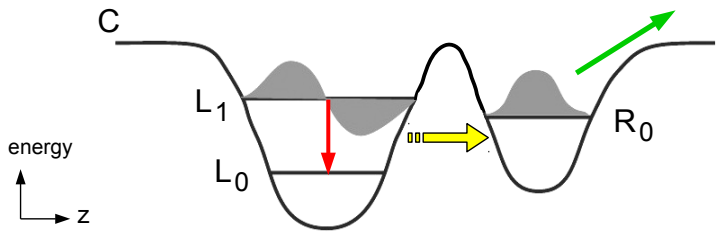

Figure 2: QD-ICD for the quasi one-dimensional model with continuum C only in the z direction. The figure shows the conduction band of a pair of each singly negatively charged QDs with the electrons (gray) in the decaying resonance state L_1R_0. During ICD the electron in the left dot drops into the energetically lower L_0 level. Simultaneously, the excess energy is transferred to the electron in the right dot which is consequently excited from the R_0 level into a continuum state.

the resonantly excited two-electron state L_1R_0 decays by an energy transfer from the left to the right dot, during which the one electron drops into the empty L_0-level and the second electron is simultaneously transferred into an unbound continuum state. The energy condition for ICD demands the energy level difference in the left dot $\omega = |E_{L_1} - E_{L_0}|$ to be large enough for the electron in the right dot with energy E_{R_0} to overcome the ionization barrier which is defined at zero. When also taking the Coulomb repulsion between both electrons into account, ICD is enabled already for $\omega + V_{\mathrm{Coul}} > |E_{R_0}|$.

For well-separated QDs the kinetic energy of the ICD electron falls below the Coulomb barrier, such that it was found to predominantly escape to the right for a distance of 87 nm between the dots.[53] However, electrons were also found left from the QDs as tunneling through the Coulomb blockade is possible. The distance dependent total decay rate $\Gamma(R)$ shows oscillatory behavior around R^{-6}, which was not observed for atomic clusters.[14],[29] This is explained as follows: the ICD electron reflected from the Coulomb barrier can be trapped again in the resonance and re-emitted, which in consequence causes a slower decay. The probability for recapture depends on the chance for tunneling, as well as on the structure of the continuum states near the right dot which alternates with R.[53]

The decay time of ICD in the QDs was found to be in the picosecond regime (133 ps for a distance of 87 nm between QDs made of GaAs),[53] which is about three to four orders of magnitude longer than in molecules and atoms.[24] Still, ICD shows a higher efficiency than the photon decay in QDs, which is in the range of nanoseconds.[53],[63] Furthermore, vibrational relaxation is not able to compete with ICD, since the decay time for acoustic phonons would be within nanoseconds and the coupling to longitudinal phonons is ruled out as excitation energies are small enough to prevent inter-band transitions.[64] There have been detailed studies on the ICD performance via geometry control of the QDs to further optimize the process.[62],[65]

Utilizing time-dependent methods in form of the multiconfiguration time-dependent Hartree (MCTDH) algorithm[66],[67] does not only make the evolution of the system visible, but also allows to incorporate time-dependent electro-magnetic fields. With that, it was possible to study

the complete light-induced process like it would correspond to an experimental procedure – from the resonant excitation of the ground state by a laser to the ensuing decay by ICD.[54] A π-pulsed laser excitation in the far-infrared (IR) regime and of linear z-polarization was used to invert the ground state L_0R_0 population into the resonance state L_1R_0.[54] After the pulse, solely the decay by ICD determines the electron dynamics.

For the pure decay from the resonance state the ICD electron spectrum gives a single peak Lorentzian shape, whereas, for the π-pulse induced ICD the spectrum takes the form of a Fano profile.[54] Such a profile arises if more than one decay channel is present, which is here besides ICD the direct ionization by the laser.[68] In an experiment the electron spectra could be compared to photocurrent spectra.[69]

The continuous excitation of the two electron system with a monochromatic laser focused on the left QD revealed Rabi oscillations,[70],[71] i.e., sustained inversions of the electron population between L_0 and L_1, however overlaid with the simultaneous decay by ICD.[54]

There exists a high interest in the interaction of QDs with electromagnetic fields in the spectral ranges of IR and visible light.[72]–[76] This comes from the potential applications for opto-electronic devices, e.g., for QD lasers[77] or single-photon emitters.[78] The herein discussed QD-ICD, which becomes operative after IR excitation, is seen in the device application for the registration of very weak low energetic electromagnetic radiation of specific wavelength, i.e., as IR photodetector. Existing QD IR-photodetectors (QDIP) register the photocurrent after the transition of an electron from a discrete QD level into the continuum.[79]–[82] However, the direct ionization of a bound electron from an isolated QD is relatively inefficient as the wave function overlap of a bound and a continuum function is comparably low. With ICD as the fundamental decay channel, the QDIP could be improved by enhancing the conversion of IR light into electron current. By adding a second QD the intermediate step of photon absorption brings the system into the metastable resonance state which has a significantly larger overlap with the ground state, and then efficiently decays by electron emission.

This thesis shall increase the insight into the dynamics of the QD-ICD process as presented above and in prior studies.[53],[54] At the same time, the anticipated experimental feasibility as well as the possible device application as a QDIP shall be kept in mind. Therefore, different possibilities for controlling the QD-ICD by means of the exciting laser are checked. Besides the laser focus, which has been introduced in earlier studies,[54] new control options are presented here, that are the intensity as well as the polarization of the laser. Furthermore, a second continuum dimension is introduced, which enables to treat a completely new type of QDs in a two-dimensional lateral arrangement. In order to optimize the ICD process in the QDs new analyzing tools have been developed that help to trace back the path of the electrons during the excitation and the ensuing decay.

The thesis is structured as follows: In Sec. 2 a theoretical overview is given. It covers the physics of QDs and introduces the specific models studied here as well as their interaction with light (Sec. 2.1). Moreover, the MCTDH wave function approach used for the electron dynamics calculations is presented (Sec. 2.2), and the computational methods are elaborated on (Sec. 2.3). The summary can be found in Sec. 3 and an overview of the publications is given in Sec. A.

2 Theoretical Background

2.1 Quantum dots and laser control

This section introduces the physics of quantum dots (QD),[83]–[85] and presents the models that were used for studying the QD-ICD. Moreover, the interaction with light is described in regard to the laser control options. Finally, a collection of the analytical tools is given.

2.1.1 Towards zero-dimensional semiconductors

The free electron

A single electron in vacuum, where it is not exposed to any interactions and solely carries kinetic energy, represents the most simple electronic system. Its state can be described by a plane wave that is a function of space $\vec{r} = (x, y, z)$ and time t,

$$\psi = e^{i(\vec{k}\cdot\vec{r}-\omega t)}, \tag{2}$$

with wave vector $\vec{k} = (k_x, k_y, k_z)$ and frequency ω. Within the quantum mechanical treatment of the electron the particle-wave duality becomes apparent. On the one hand, the time-independent Schrödinger equation

$$\hat{H}\psi = E\psi, \tag{3}$$

with the time-independent Hamilton operator for the free electron $\hat{H} = |\vec{\hat{p}}|^2/(2m_e)$, the electron mass m_e, momentum operator $\vec{\hat{p}} = \hbar\vec{\hat{k}} = -i\hbar\vec{\nabla}$, and nabla operator $\vec{\nabla} = (\frac{\partial}{\partial_x}, \frac{\partial}{\partial_y}, \frac{\partial}{\partial_z})$, yields the eigenenergies $E = \hbar^2|\vec{k}|^2/(2m_e)$ as for a classical particle. The wave-like behavior of matter was proposed by de Broglie who stated that particles can be connected to a wavelength $\lambda = 2\pi/|\vec{k}|$.[86] On the other hand, the time-dependent Schrödinger equation

$$i\hbar\frac{\partial}{\partial t}\psi = \hat{H}\psi, \tag{4}$$

applied for the time-independent system and together with Eq. (3), gives the energy $E = \hbar\omega$. This is also known for photons and shows the particle-like behavior of the electron.

Electrons within solid bodies

The research field of solid state bodies as part of condensed matter physics treats materials that are built of a great number of densely packed atoms. The main interest lies in crystalline structures that are assembled by regularly arranged atoms. These structures can be described in terms of three-dimensional periodic lattices. The lattice sites are defined at the equilibrium position of the spherically symmetric atomic core potentials. The latter result from the heavy positively charged atomic nuclei that are screened by the light cloud of negatively charged inner shell (core) electrons.

At finite temperature the core potentials vibrate about their equilibrium position. These lattice vibrations can be described by quantized harmonic oscillators leading to the concept of

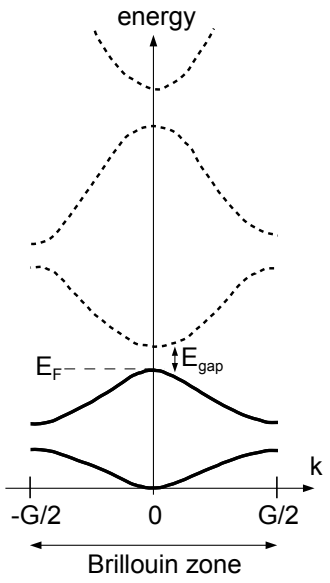

Figure 3: A generic band structure in the first Brillouin zone of a one-dimensional homogeneous crystal lattice at $T = 0$. The valence bands (solid lines) are filled up to the Fermi level E_F and the conduction bands (dotted lines) are empty. The energy gap E_{gap} between the top of the most outer valence band and the minimum of the conduction band is the minimum energy that is required to form an electron current.

phonons. The interaction with phonons is taken as negligible in this thesis, since the decay in the systems under investigation is faster by ICD than by a vibrational relaxation, cf. Sec. 1. At zero temperature the lattice is static and can be mathematically described in the $\vec{r}$-space. It was found to be convenient to describe it also in the Fourier transformed space, i.e., the reciprocal or $\vec{k}$-space, where the lattice sites are given at the *reciprocal lattice* vectors $\vec{G}$. The *first Brillouin zone* (FBZ) defines the range of reciprocal space of the homogeneous crystal that lies closer to $\vec{G} = 0$ than to any other lattice point $\vec{G} \neq 0$. The FBZ repeats with the periodic lattice and is thus representative for the whole structure.

The relatively few outer shell (valence) electrons take part in the cohesion, that means in the inter-atomic forces that hold the crystal together. For example, *covalent bonds* are built between the valence electrons of neighboring atoms. Similarly, *metallic bonds* exist between valence electrons, but the bond charges can move easily and are shared over the whole structure. On the other hand, *ionic bonds* are established due to electrostatic attraction between oppositely charged ions.

The differently bonded crystals have unequal ability for conduction of an electronic current, which can be understood by introducing the concept of *energy bands*, cf. Fig. 3. The high density of valence electron states in a crystal forms the *valence bands*. Instead of describing all the electrons in the valence band, one oftentimes rather only treats the empty states, so-called *holes*. Another energy band is formed by continuum states, i.e., states that energetically lie above the localized states of the valence band and extend over the whole crystal. Electrons in these states are able to

form a current flow, hence this second band is known as *conduction band*. In neutral compounds all valence states are filled with electrons at zero temperature and the highest occupied state describes the so-called *Fermi level* with energy E_F. The energy difference between the Fermi level and the conduction band minimum is called *energy band gap*. Note that minimum and maximum can be at same or different $|\vec{k}|$, which corresponds to a direct or indirect gap. For metals this gap is zero, that means valence and continuum states lie in the same band and electrons can easily spread over the whole structure. Semiconductors, which are crystals formed by covalent bonds, have a nonzero energy gap. This means that an excitation by for example an external bias voltage or light is necessary to provide sufficient energy for the valence electrons to transfer into a conducting state. In this regard, one distinguishes between type-I and type-II semiconductors depending on whether they posses a direct or indirect band gap. For very large band gaps the crystal becomes insulating, that means the electrical resistivity gets very high and no current can flow under normal electric potential difference. This is the case for ionic bonded systems.

To describe a single electron including all interactions in a rather large crystal is very demanding. However, the problem can be simplified by fitting the mass of the electron within the crystal potential such that it seems as if the electron was moving in vacuum with a different and material specific mass m^*. Close to the minimum or maximum of a parabolic shaped energy band it can be approximated by

$$m^* = \frac{\hbar^2}{d^2E/dk^2}, \tag{5}$$

for which the energy bands are given by the dispersion relation

$$E(\vec{k}) = E_0 \pm \frac{\hbar^2|\vec{k}|^2}{2m^*}. \tag{6}$$

This concept is known as the *effective mass approximation*, which is valid in the region of the local extremum E_0 of the respective energy band. Thus, the electron describes a different effective mass within different bands.

Nano-sized semiconductor heterostructures - quantum wells

Consider a semiconductor material A that is of narrower band gap than another material B, thus $E_{\text{gap}}^{\text{A}} < E_{\text{gap}}^{\text{B}}$. If a sufficiently thin layer of A ($\approx$ nanometers) is enclosed by a thick barrier material B, quantum phenomena like the *quantum size effect* become apparent. The B-A-B band alignment gives a finite confining potential within one dimension called a *single quantum well*. The states within the confining dimension of the well are discrete, that means the energy is not a continuous function of the wave vector anymore, but rather of an integer quantum number, as shown in Fig. 4. Since the confining potential is finite, the bound state wave functions within A reach into the barrier regions of B.

There exist also states that lie energetically within the continuum, thus they are unbound, but are still localized in the quantum well region. These states are called *resonance continuum*

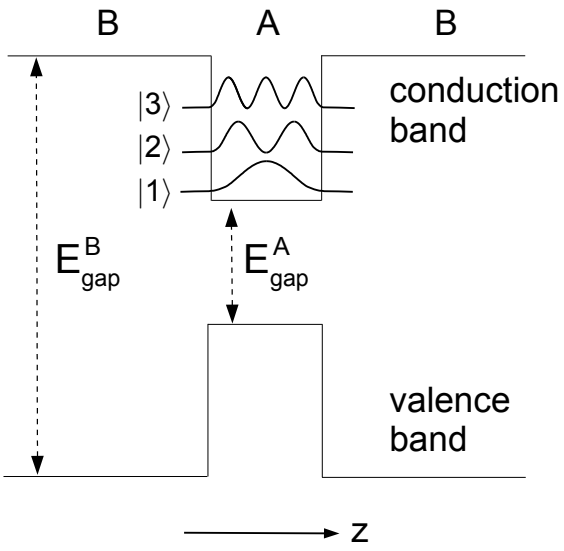

Figure 4: Quantum well band structure with discrete electron states $|n\rangle$ in the conduction band of A. Note that the electron densities are non-zero within the barriers B as the confining potential is finite. The discrete hole state in the valence band are not depicted.

states or virtual levels. Electrons in a resonance state can more easily transfer into neighboring continuum states than real bound states.

Assume the confinement is along the z-direction, then the potential extends infinitely in x and y with states of continuous energy. Because of the confinement in the one dimension, the states within the quantum well are referred to as two-dimensional states. The total energy $E = E_n + E_{x,y}$ gives energy domains that are called *subbands*.

More complex structures are possible, e.g., *multiple quantum wells* as a collection of non-interacting single quantum wells, or *double quantum wells* and *superlattices* where interaction between the wells takes place.

Further potential confinement - Quantum wires and dots

An electron in a quantum well can move freely within the two non-confining dimensions x and y. By adding another confining dimension, for example in y, the well turns into a one-dimensional *quantum wire*, for which states along y and z are discrete and x is the only continuum dimension.

Finally, confinement in all three spatial dimensions leads to zero-dimensional objects called *quantum dots* (QD). Within the QD structure only discrete states exist. There exist a range of common techniques for producing QDs. One of them is for example through *self-assembly.*[87]–[89] There, a thin semiconductor layer is grown on top of another semiconductor substrate. Due to lattice mismatch of the two materials the thin layer spontaneously arranges into small ideally pyramid-shaped islands which group in a lateral formation on a two-dimensional plane. This happens through an elastic response. The lattice constant of the thin layer is reduced in the plane to fit the lattice of the substrate, followed by an extended lattice constant along the growth

direction. This technique became known by the name "Stranski-Krastanov" growth mode.[90] In other methods, the QDs are electrostatically confined: a two-dimensional electron gas is created between two thin semiconductor films of different band gap, and then further confined by metallic gates to define the dot regions.[91], [92] QDs that have been chemically synthesized in solutions are known by the name nanocrystals or colloidal dots and have a spherical symmetry.[93]

2.1.2 Quantum dot model system

The quantum mechanical system, for which the QD-ICD by means of electron dynamics is studied, consists of a pair of well separated GaAs QDs surrounded by some barrier material of similar effective mass. Each dot is charged by a single electron. Besides the fact that the two QDs shall be of different size in order to fulfill a specific energy requirement for ICD, the dots are rather unspecific. Hence, a relatively simple model is applied.

The QD pair that has been studied in previous works[53], [54] was described by a quasi one-dimensional model potential that allows electronic motion in only one continuum direction and shows strong confinement in the transversal directions. This model represents the case where the two QDs are embedded in a one-dimensional nanowire. The following function models the conduction band of the dots connected to the surrounding barrier region,

$$\hat{V}_{\mathrm{QD}}^{\mathrm{wire}}(x,y,z) = -\sum_{j=L,R} D_j \exp\left\{-b_j[(\hat{z}-z_j)^2]\right\} + \hat{V}_{\mathrm{HO}}(x,y). \tag{7}$$

It contains the sum of two negative Gaussians aligned in the z direction. The sum runs over the two QDs j called "left" (L) and "right" (R) that are centered at $z_{L,R} = \mp 43.34\,\mathrm{nm}$, respectively. The dot potentials are of the different depths $D_L = 10.30\,\mathrm{meV}$ and $D_R = 8.24\,\mathrm{meV}$. The surrounding barriers are set to $V = 0$ which also corresponds to the ionization threshold. The width parameters $b_{L,R} = 4\ln(2)/r_{L,R}^2$ are defined by the full widths at half maximum $r_L = 36.08\,\mathrm{nm}$ and $r_R = 18.04\,\mathrm{nm}$ of the dots. For the transversal directions strong confinement is assumed in form of continuum-free harmonic oscillator potentials[53], [54], [62]

$$\hat{V}_{\mathrm{HO}}(x,y) = \frac{1}{2} m_e\, \omega_\perp^2\, (\hat{x}^2 + \hat{y}^2)\,, \tag{8}$$

with the frequency of the transversal potential $\omega_\perp = 10.30\,\mathrm{meV}$. The Fig. 5 (a) shows the QDs-in-a-wire potential Eq. (7).

The potential Eq. (7) can be extended by another continuum dimension, say x, in form of a Gaussian centered at zero,

$$\hat{V}_{\mathrm{QD}}^{\mathrm{lat.}}(x,y,z) = -D \sum_{j=L,R} \exp\left\{-b_j[(\hat{z}-z_j)^2 + \hat{x}^2]\right\} + \hat{V}_{\mathrm{HO}}(y), \tag{9}$$

as depicted in Fig. 5 (b). This makes electronic motion now possible in x and z, which corresponds to laterally arranged QDs (lat.) on a two-dimensional wetting layer. The two cylindrically-symmetric dots of the potential Eq. (9) are of equal depth $D = 21.67\,\mathrm{meV}$ and centered at

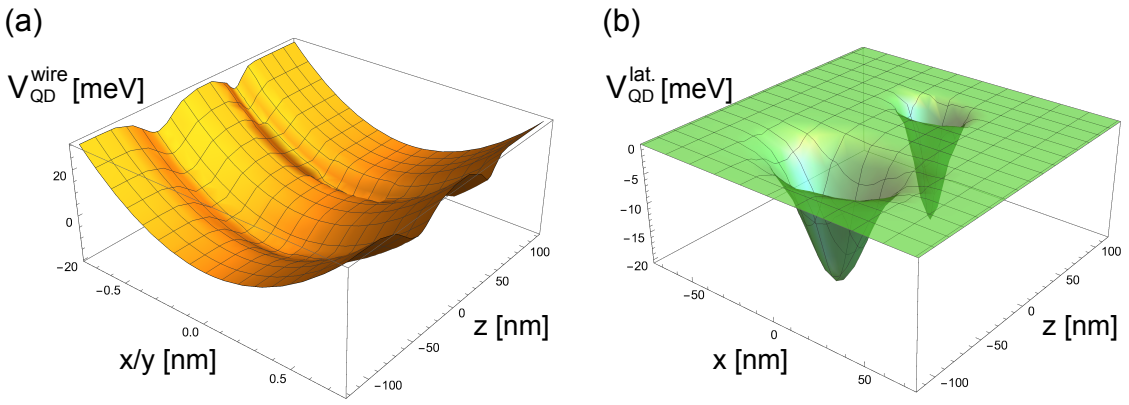

Figure 5: Comparison of the QD model potentials. (a) QDs embedded in a nanowire with one-dimensional continuum in z and strong confinement in the transversal directions x and y. (b) Laterally arranged QDs on a two-dimensional wetting layer and strong confinement in the third dimension.

$z_{L,R} = \mp 54.18\,\mathrm{nm}$. The inter-dot distance was here slightly increased in comparison to Eq. (7) in order to keep the electron density sufficiently separated. The width parameters are as above. Again, the confinement in the third direction is assumed to be strong as comprised in $\hat{V}_{\mathrm{HO}}(y)$.

The electronic Hamiltonian for the pair of singly-charged QDs, either embedded in a nanowire or in lateral arrangement, looks as follows,

$$\hat{H}_{\mathrm{el}}^{\mathrm{wire/lat.}} = \sum_{i=1}^{2} \left[-\frac{\hbar^2}{2m_e} \vec{\nabla}_i^2 + \hat{V}_{\mathrm{QD}}^{\mathrm{wire/lat.}}(x_i, y_i, z_i) \right] + \hat{V}_{\mathrm{Coul}}(r_{12}). \tag{10}$$

It contains the kinetic energies of the two electrons $i = 1, 2$ with nabla operator $\vec{\nabla}_i = (\frac{\partial}{\partial x_i}, \frac{\partial}{\partial y_i}, \frac{\partial}{\partial z_i})$, the QD potential Eqs. (7) or (9), as well as the electron Coulomb interaction. The latter is defined as

$$\hat{V}_{\mathrm{Coul}}(r_{12}) = \kappa\, \hat{r}_{12}^{-1}, \tag{11}$$

with the prefactor $\kappa = e^2/(4\pi\epsilon_0\epsilon)$ that contains the elementary electron charge e, the vacuum electric permittivity ϵ_0 and the relative material specific permittivity ϵ, as well as the distance between the electrons

$$r_{12} = |\vec{r}_1 - \vec{r}_2| = \sqrt{(x_1 - x_2)^2 + (y_1 - y_2)^2 + (z_1 - z_2)^2}. \tag{12}$$

To avoid singularities a regularized form of the Coulomb interaction can be used,

$$\hat{V}_{\mathrm{Coul}}^{\mathrm{reg}}(r_{12}) = \kappa \left(\hat{r}_{12}^2 + a^2 e^{-b\,\hat{r}_{12}} \right)^{-1/2}. \tag{13}$$

The parameters $a = 1.1\,\mathrm{nm}$ and $b = 9.2\,\mathrm{nm}^{-1}$ were chosen to not alter the Coulomb potential anywhere except at the coalescence point of both electrons, where the electrons are very unlikely to be found.[53]

For the QDs in a nanowire, it has been shown that the transversal directions within the Coulomb interaction can be accounted for by integrating over x and y beforehand.[61] The result is the effective Coulomb potential[94]

$$\hat{V}_{\mathrm{Coul}}^{\mathrm{eff}}(\zeta) = \sqrt{\frac{\pi}{2}}\frac{\kappa}{l} e^{\hat{\zeta}^2} \operatorname{erfc}(\hat{\zeta}) \,, \tag{14}$$

with the confinement scale $l = \sqrt{\hbar/(m_e\,\omega_\perp)}$, the inter-electron distance parameter $\zeta = |z_1 - z_2|/(\sqrt{2}l)$, and the complementary error function erfc. The potential of strong confinement in x and y Eq. (8) can be neglected since excitations in these directions are very unlikely with the energies appearing here. It is then possible to perform calculations solely in the continuum z dimension. This gives the same results as computing with all three dimensions and additionally reduces the computational effort. However, the effective potential where only y is integrated over is not as trivial. Thus, for laterally arranged QDs the regularized Coulomb potential Eq. (13) is used and y is simply dropped in the Coulomb potential as well as the QD potential. It was argued that differences in the calculations for either a quasi (including y) or pure two-dimensional system would be of numerical nature, if at all.

The time-independent Schrödinger equation,

$$\hat{H}_{\mathrm{el}}\ |\alpha\rangle = E_\alpha\ |\alpha\rangle, \tag{15}$$

can be solved either for the QDs in a nanowire or the laterally arranged dots, Eq. (10). This yields the two-electron eigenfunctions $|\alpha\rangle$, or in other words the electronic structure of the considered QD system,

$$|\alpha\rangle^{\mathrm{wire}} = \begin{cases} |n_{z_1}, n_{z_2}\rangle & \text{with } n_{z_1} \neq n_{z_2}, \\ |n_{z_1}, \varepsilon\rangle, & \\ |\varepsilon, \varepsilon'\rangle & \text{with } \varepsilon \neq \varepsilon', \end{cases} \tag{16}$$

$$|\alpha\rangle^{\mathrm{lat.}} = \begin{cases} |m_{x_1} n_{z_1}, m_{x_2} n_{z_2}\rangle & \text{with } m_{x_1} \neq m_{x_2} \text{ or } n_{z_1} \neq n_{z_2} \\ \dots & \text{other continuum configurations}, \end{cases} \tag{17}$$

where m_x and n_z label the discrete single-particle levels in the dots in x and z direction, and $\varepsilon > 0$ is the kinetic energy of an electron in a continuum state in either direction. The two-electron states can be combinations of bound states, continuum states, or a mixture of both. Due to the Pauli principle and the choice of spin-triplet states not all two-particle states are available, cf. Eqs. (16) and (17). This is to keep the total wave function antisymmetric, cf. Sec. 2.2.4.

2.1.3 Light-matter interactions

The electron dynamics can be studied by solving the time-dependent Schrödinger equation,

$$i\hbar\frac{\partial}{\partial t}\Psi(t) = \hat{H}\Psi(t). \tag{18}$$

If the system is initially in the decaying resonance state, $\hat{H}$ is the time-independent electronic Hamiltonian of Eq. (10). Otherwise, the resonance state can be prepared by applying a resonant laser pulse on the ground state.[54] In this case the Hamiltonian becomes time-dependent,

$$\hat{H}(t) = \hat{H}_{\text{el}} + \hat{H}_{\text{field}}(t). \tag{19}$$

In the semiclassical dipole approximation the additional time-dependent part for the electron-field interaction looks as follows,

$$\hat{H}_{\text{field}}(t) = -\vec{\mathcal{E}}(t)\cdot\vec{\hat{\mu}}\ . \tag{20}$$

The scalar product in Eq. (20) is taken between the dipole moment vector,

$$\vec{\hat{\mu}} = \begin{cases} -e\sum_{i=1}^{2}\left(\vec{\mathbf{e}}_z\hat{z}_i\right) & \text{(wire)},\\ -e\sum_{i=1}^{2}\left(\vec{\mathbf{e}}_x\hat{x}_i + \vec{\mathbf{e}}_z\hat{z}_i\right) & \text{(lat.)}, \end{cases} \tag{21}$$

and the time-dependent electric field vector,

$$\vec{\mathcal{E}}(t) = \eta\, g(t)\,\Theta(t_{\text{pulse}} - t)\begin{cases} \vec{\mathbf{e}}_z\,\cos\left(\omega t+\varphi\right) & \text{(wire)},\\ \left[\vec{\mathbf{e}}_x\,\varepsilon_x\,\sin\left(\omega t+\varphi\right) + \vec{\mathbf{e}}_z\,\varepsilon_z\,\cos\left(\omega t+\varphi\right)\right] & \text{(lat.)}, \end{cases} \tag{22}$$

with the field strength η, photon energy ω, phase φ and the unit vectors $\vec{\mathbf{e}}_{x/z}$. The phase is kept constant $\varphi = 0$ for all calculations. The laser intensity is related to the field via $I = 0.5\,c\,n_r\,\epsilon_0\epsilon\,|\vec{\mathcal{E}}|^2$, where c is the speed of light in vacuum and n_r the refractive index. The shape of the pulse is given by the envelope function $g(t) = \sin^2\left(\pi t/t_{\text{pulse}}\right)$ with the pulse length t_{pulse}. The Heaviside function Θ sets the field to zero after the pulse. When calculating with a single continuum dimension the laser is linearly polarized along z. The ellipticity ε_x and ε_z for the polarization of the laser field in x and z is introduced for calculations in the plane of laterally arranged QDs. If either $\varepsilon_x = 0$ or $\varepsilon_z = 0$, the light is linearly polarized. Exciting with equal field components in x and z, i.e., $\varepsilon_x = \varepsilon_z$, will result in light of circular polarization. Accordingly, elliptically polarized light is obtained when $\varepsilon_x \neq \varepsilon_z$ and $\varepsilon_x \wedge \varepsilon_z > 0$.

The amount of population inversion from ground to resonance state can be controlled by the intensity and the pulse length of the laser. A resonant pulse that completely depopulates the ground state and maximally populates the resonance state is called a *π-pulse* and corresponds to 1/2 of a so-called *Rabi-cycle*. Otherwise, for continuous resonant excitations the populations in the two states are determined by Rabi oscillations, i.e., ongoing population inversions. Under the *rotating wave approximation* the populations of a two-level system are described by the following time-dependent expressions for the ground level $|0\rangle$ and the excited level $|1\rangle$,[95]

$$P_0(t) = \cos^2\left(\frac{\Omega_{\Re}t}{2}\right), \tag{23}$$

$$P_1(t) = \sin^2\left(\frac{\Omega_{\Re}t}{2}\right). \tag{24}$$

The Rabi frequency $\Omega_{\mathfrak{R}}$ is defined by the cycle duration $T = 2\pi\Omega_{\mathfrak{R}}^{-1}$. For the two-electron QD pair, Rabi oscillations between ground state (GS) and resonance state (RS) compete with the exponential decay of the resonance state via ICD into a continuum state as well as with direct ionization processes, cf. Sec. 1. For low laser intensities, i.e., within the regime of single-photon excitations into a limited number of continuum states, the ground and resonance state populations can therefore be approximated by,

$$P_{\mathrm{GS}}(t) = e^{-(\Gamma_{\mathrm{ICD}}+\Gamma_{\mathrm{ion},\eta})t}\cos^2\left(\frac{\Omega_{\mathfrak{R}}t}{2}\right), \tag{25}$$

$$P_{\mathrm{RS}}(t) = e^{-(\Gamma_{\mathrm{ICD}}+\Gamma_{\mathrm{ion},\eta})t}\sin^2\left(\frac{\Omega_{\mathfrak{R}}t}{2}\right). \tag{26}$$

The exponential factor introduces the decay via ICD with rate Γ_{ICD} as well as direct ionization with the field-dependent rate $\Gamma_{\mathrm{ion},\eta}$. Furthermore, the Rabi frequency becomes time-dependent and is given by the following expression,

$$\Omega_{\mathfrak{R}}(t) = \mu\eta g(t). \tag{27}$$

The transition dipole moment $\mu = |\langle RS|\vec{\hat{\mu}}|GS\rangle|$ gives a measure of how well the transition between the two states is performed under excitation with the laser of given polarization. The time dependence of the Rabi frequency results from the envelope function $g(t) = \sin^2(\pi t/t_{\mathrm{pulse}})$ used for the shape of the pulse in Eq. (22). If all population within the QDs shall be excited from the ground state into the resonance state by the end of the pulse, it requires the fulfillment of

$$\int_0^{t_{\mathrm{pulse}}} \Omega_{\mathfrak{R}}(t)dt = \pi\,, \tag{28}$$

according to Eqs. (26) and (27). Thus, a relation for the field strength in dependence on the pulse length is obtained, which describes the so-called π-pulse condition,

$$\eta_\pi = \frac{2\pi}{\mu\, t_{\mathrm{pulse}}}\,. \tag{29}$$

Choosing a short pulse length results in high field strengths in favor for direct ionization processes. Otherwise, for small field strengths a long pulse length is needed, such that ICD becomes faster than the pulse and cannot be detected anymore. Hence, the optimal laser parameters are found when the resonance state is populated to a maximum. However, the ionization processes cannot be completely avoided, such that the maximum of the resonance state population will never reach a value of one.

Besides intensity and ellipticity, the focus of the laser was studied here as well to control the ICD process in the QDs. Mathematically, the laser can be adjusted in z onto the left QD by multiplying the field Hamiltonian by a spatial Heaviside function,

$$\hat{H}'_{\mathrm{field}}(t) = \Theta(-z)\hat{H}_{\mathrm{field}}(t). \tag{30}$$

Thus, the laser solely acts on the negative z-axis where the left dot is located. Experimentally, this can be achieved by the use of shadow masks.[96]

2.1.4 Analysis of the electron dynamics

With the knowledge of the wave function as well as the single- and two-electron states, a range of observables can be analyzed. The ones that were used for determination of the electron dynamics in the QD-ICD are presented in the following.

Firstly, the populations of the two-electron states $|\alpha\rangle$, Eqs. (16) and (17), are obtained from the expectation value of the projection operator $\hat{P}_\alpha = |\alpha\rangle\langle\alpha|$ as

$$P_\alpha(t) = \langle\Psi(t)|\hat{P}_\alpha|\Psi(t)\rangle = |\langle\alpha|\Psi(t)\rangle|^2. \tag{31}$$

The decay of the resonance state via ICD gives a population proportional to $e^{-\Gamma_{\mathrm{ICD}}t/\hbar}$ for intermediate times, from which the decay rate Γ_{ICD} can be obtained. The inverse of the rate gives the decay time $\tau_{\mathrm{ICD}} = \hbar\,\Gamma_{\mathrm{ICD}}^{-1}$.

Due to the normalization condition, the sum of populations in all the two-electron states must equal one at all times. Thus, for the QDs-in-a-wire states Eqs. (16) with the levels $n_z = L_0$, L_1 and R_0, cf. Sec. (1), it must be

$$\begin{aligned} 1 &= \sum_\alpha P_\alpha(t) \\ &= P_{L_0R_0}(t) + P_{L_1R_0}(t) + P_{L_0C}(t) + P_{L_1C}(t) + P_{R_0C}(t) + P_{CC'}(t) \\ &= P_{L_0R_0}(t) + P_{L_1R_0}(t) + P_C(t) \end{aligned} \tag{32}$$

for which $P_{n_z'n_z}(t) = P_{n_zn_z'}(t)$ or $P_{n_zC}(t) = P_{Cn_z}(t)$ is valid. Here, we introduced the short notation for the continuum terms $P_{n_zC}(t) = \int d\varepsilon P_{n_z\varepsilon}(t)$, or for two continuum electrons $P_{CC'}(t) = \iint d\varepsilon d\varepsilon' P_{\varepsilon\varepsilon'}(t)$. Moreover, $P_C(t)$ combines all continuum populations, thus gives the probability for at least one electron to be in a continuum state. Note that the L_0L_1 configuration does not appear here. This is because the electrons are supposed to be initially in different QDs and from there tunneling is ruled out, since the dots are well separated and the applied excitation energies are low enough.

One may equally calculate the one-electron level populations by a projection on the wave function. For the QDs-in-a-wire system, Eq. (10) with QD potential Eq. (7), this looks as follows,

$$P_{n_z}(t) = 2|\langle n_z|\mathbb{1}_2|\Psi(t)\rangle|^2, \tag{33}$$

where the prefactor two accounts for the two identical particles. For inclusion of the coordinate of the second electron the projection on the two-particle identity is necessary,

$$\mathbb{1}_2 = \frac{1}{2}\sum_{n_z,n_z'} |n_z,n_z'\rangle\langle n_z,n_z'| + \sum_{n_z}\int d\varepsilon\,|n_z,\varepsilon\rangle\langle n_z,\varepsilon| + \frac{1}{2}\iint d\varepsilon d\varepsilon'\,|\varepsilon,\varepsilon'\rangle\langle\varepsilon,\varepsilon'|. \tag{34}$$

To evaluate the overlap of one- and two-particle states, the antisymmetric two-electron eigenstates can be approximated by two-term products of single-particle solutions,

$$|n_z,n_z'\rangle = \frac{1}{\sqrt{2}}\left(|n_z'\rangle|n_z\rangle - |n_z\rangle|n_z'\rangle\right), \tag{35}$$

which holds also for the continuum states. Thus, by inserting Eq. (34) with the usage of Eq. (35), Eq. (33) turns into

$$P_{n_z}(t) = \sum_{n'_z} P_{n'_z n_z}(t) + P_{n_z C}(t). \tag{36}$$

This yields the following relations for the single-electron state populations expressed via the two-electron states,

$$P_{L_0}(t) = P_{L_0 R_0}(t) + P_{L_0 C}(t), \tag{37}$$

$$P_{L_1}(t) = P_{L_1 R_0}(t) + P_{L_1 C}(t), \tag{38}$$

$$P_{R_0}(t) = P_{L_0 R_0}(t) + P_{L_1 R_0}(t) + P_{C R_0}(t). \tag{39}$$

With Eqs. (37)-(39) one can conclude on continuum state populations just by knowing the bound and resonance state populations. This is however only possible if absorbing boundaries are absent, since they remove continuum state density, as described in Sec. (2.3.5).

The same principles of Eqs. (31)-(33) also hold for laterally arranged QDs. In this case however, the four degrees of freedom (x, x', z, z') and the many more combinations of bound states make the analysis of the single populations way more complicated.

Secondly, the electron density of a specific state can be calculated as

$$\rho_\alpha(z) = \int |\Phi_\alpha(z, z')|^2 \mathrm{d}z', \tag{40}$$

$$\rho_\alpha(x, z) = \iint |\Phi_\alpha(x, x', z, z')|^2 \mathrm{d}x' \mathrm{d}z', \tag{41}$$

or likewise the time-dependent electron wave function density is

$$\rho(z, t) = \int |\Psi(z, z', t)|^2 \mathrm{d}z', \tag{42}$$

$$\rho(x, z, t) = \iint |\Psi(x, x', z, z', t)|^2 \mathrm{d}x' \mathrm{d}z'. \tag{43}$$

The densities are analyzed for the QDs in the wire along the z direction, Eqs. (40) and (42), or within the plane in x and z direction, Eqs. (41) and (43).

Thirdly, to calculate quantum fluxes one can take advantage of the complex absorbing potentials (CAP),[97]–[100] cf. Sec. (2.3.5). The flux into a CAP along dimension x or z and left ("−") or right ("+") from the system can be calculated as expectation value of the CAP operator, Eq. (105), integrated over a defined time interval δt and summed over both particles i,

$$F_\pm^{x/z} = \sum_{i=1,2} \int_{t_0}^{t_0+\delta t} \langle \Psi(t) | \hat{W}^\pm_{x_i/z_i} | \Psi(t) \rangle \, \mathrm{d}t \ . \tag{44}$$

The total flux is then simply obtained by summing over the partial fluxes,

$$F = \begin{cases} F_-^z + F_+^z & \text{(wire)} \\ F_-^x + F_+^x + F_-^z + F_+^z & \text{(lat.)} \ . \end{cases} \tag{45}$$

Finally, the electron spectrum can be calculated from the crosscorrelation function $c_\alpha(t) = \langle\alpha|\Psi(t)\rangle$ of the decaying state α and for sufficiently long propagation times as follows,

$$\sigma_\alpha(E) = 2E \int_0^T \mathrm{Re}[\, c_\alpha(t) e^{i(E+E_\alpha)t/\hbar}\,]\,\mathrm{d}t\ . \tag{46}$$

As discussed in Sec. 1, electron spectra for light-induced ICD give Fano profiles because of additional decay channels via direct ionizations. The ICD rate can be obtained from fitting the general Fano line shape[68]

$$\sigma_\alpha^{\mathrm{Fano}}(E) = \frac{1}{1+q^2}\,\frac{[q\cdot\Gamma_{\mathrm{ICD}}/2 + (E-E_\alpha)]^2}{(\Gamma_{\mathrm{ICD}}/2)^2 + (E-E_\alpha)^2} \tag{47}$$

onto the spectrum centered at the decaying state energy E_α. The spectrum is normalized by the factor $(1+q^2)^{-1}$. The Fano profile parameter q determines the relative importance of ICD in comparison to direct ionizations. In general, the impact of direct ionization increases for decreasing q.

All calculations were usually performed in atomic units (a.u.). Afterwards, the physical quantities were converted into the material specific International System (SI) Units of GaAs based on the effective mass approximation,[101] with the effective electron mass $m^*_{\mathrm{GaAs}} = 0.063$ and the dielectric constant $\kappa_{\mathrm{GaAs}} = 12.9$.[102] Note that GaAs is the QD material and electrons in the surrounding barrier material are assumed to be of similar effective mass.

2.2 Wavefunction-based electron dynamics

In this section the multiconfiguration time-dependent Hartree (MCTDH) method[66],[67] for high-dimensional quantum dynamics shall be introduced as it has been applied in this thesis to study the electron dynamics for the QD-ICD process. In the following, the MCTDH method is explained based on the standard and the time-dependent Hartree method.

2.2.1 The standard method

As solution to the time-dependent Schrödinger equation (18), let us consider an f-dimensional spatial wave function, which can be expressed in Dirac notation as follows,

$$\Psi(q_1, q_2, \ldots, q_f, t) = \langle q_f| \ldots \langle q_2|\langle q_1|\Psi(t)\rangle. \tag{48}$$

The f degrees of freedom (DOF) are described by the coordinates $q_{1\ldots f}$. By inserting f times the identities $\mathbb{1}^{(\kappa)} = \sum_{j_\kappa}^{N_\kappa} |\chi_{j_\kappa}^{(\kappa)}\rangle\langle\chi_{j_\kappa}^{(\kappa)}|$, which are constructed of complete basis sets with N_κ basis functions, the wave function Eq. (48) can be expanded as

$$\langle q_f|\mathbb{1}^{(f)} \ldots \langle q_2|\mathbb{1}^{(2)}\langle q_1|\mathbb{1}^{(1)}|\Psi(t)\rangle = \sum_{j_1,\ldots,j_f} \langle q_f|\chi_{j_f}^{(f)}\rangle \ldots \langle q_2|\chi_{j_2}^{(2)}\rangle\langle q_1|\chi_{j_1}^{(1)}\rangle \underbrace{\langle\chi_{j_f}^{(f)}| \ldots \langle\chi_{j_1}^{(1)}|\Psi(t)\rangle}_{C_{j_1\ldots j_f}(t)}, \tag{49}$$

and further brought into the form

$$\Psi(q_1, q_2, \ldots, q_f, t) = \sum_{j_1}^{N_1} \ldots \sum_{j_f}^{N_f} C_{j_1\ldots j_f}(t) \prod_{\kappa=1}^{f} \chi_{j_\kappa}^{(\kappa)}(q_\kappa), \tag{50}$$

with the product of the one-dimensional time-independent basis functions $\chi_{j_\kappa}^{(\kappa)}$, for which j_κ is the index of the κ-th DOF. The time-dependent expansion coefficients $C_{j_1\ldots j_f}(t)$ as defined in Eq. (49) form the so-called C-vector. Applying the Dirac-Frenkel time-dependent variational principle[103],[104]

$$\langle\delta\Psi|\hat{H} - i\frac{\partial}{\partial t}|\Psi\rangle = 0 \tag{51}$$

for the wave function Eq. (50) yields the equations of motion for the coefficients, which circumvents to directly solve the Schrödinger equation. The advantage of this method are the numerically exact calculations, which are however limited to systems with only a small number of nuclei. That is because the computation time and memory consumption increase exponentially with f.

2.2.2 The time-dependent Hartree method

The computational effort can be reduced by moving from the exact solution of the wave function to an approximate one. A simple wave function ansatz of Hartree product form was developed,[105] where the f-dimensional wave function

$$\Psi(q_1, q_2, \ldots, q_f, t) = a(t) \prod_{\kappa=1}^{f} \varphi_\kappa(q_\kappa, t) \tag{52}$$

contains the product of orthonormal one-dimensional time-dependent basis functions $\varphi_\kappa(q_\kappa, t)$. These functions are called *single-particle functions* (SPF) and for each DOF κ one SPF is used. Eq. (52) is known as the *time-dependent Hartree* (TDH) method. Again, the Dirac-Frenkel variation principle Eq. (51) is applied and yields equations of motion for the SPFs. These are one-dimensional differential equations for each DOF κ, thus turning the f-dimensional problem Eq. (52) into f one-dimensional ones. The prefactor $a(t)$ is a rescale factor to ensure normalization. That means that the wave function ansatz is not unique. However, unique equations of motion for the SPFs can be obtained by introducing the following constraints,

$$i\langle\varphi^{(\kappa)}|\dot{\varphi}^{(\kappa)}\rangle = g^{(\kappa)}(t), \tag{53}$$

for $\kappa = 1, \ldots, f$. The arbitrary function $g^{(\kappa)}(t)$ determines the form of the equations of motion.

The TDH wave function exactly solves the time-dependent Schrödinger equation for an uncorrelated system, i.e., for uncoupled DOFs. Hence, the method becomes inaccurate for systems with strong coupling between different modes, as for example by Coulomb interactions.

2.2.3 The multiconfiguration time-dependent Hartree method

In 1990 a wave function ansatz in terms of a multiconfigurational form of the TDH method was presented by Meyer, Manthe and Cederbaum.[66], [67] It became well known as the multiconfiguration time-dependent Hartree (MCTDH) method.

The MCTDH wave function is expressed as linear combination of Hartree products,

$$\Psi(q_1, \ldots, q_f, t) = \Psi(Q_1, \ldots, Q_p, t) \tag{54}$$

$$= \sum_{j_1=1}^{n_1} \cdots \sum_{j_p=1}^{n_p} A_{j_1 \ldots j_p}(t) \prod_{\kappa=1}^{p} \varphi_{j_\kappa}^{(\kappa)}(Q_\kappa, t), \tag{55}$$

where for each particle the composite coordinates $Q_\kappa = (q_a, \ldots q_d)$ are introduced, also known as *mode combinations*.[106] Usually, not more than three coordinates are combined for the *multi-mode* SPFs $\varphi_{j_\kappa}^{(\kappa)}(Q_\kappa, t)$, or *single-mode* if $d = 1$. This leaves us with $p = f/d$ sets of d-dimensional SPFs, which lowers the computational effort. The time-dependent expansion coefficients $A_{j_1 \ldots j_p}(t)$ build the elements of the so-called A-vector.

The TDH and the standard method can be seen as special cases of the MCTDH method. By setting the number of SPFs in Eq. (55) to $n_\kappa = 1$ for all κ yields the TDH wave function Eq. (52). For $n_\kappa = N_\kappa$, i.e., using complete basis sets, the expansion is exactly like in Eq. (50). However, we may truncate n_κ, such that $n_\kappa < N_\kappa$. Hence, the A-vector is smaller than the C-vector of the standard method.

The wave function Eq. (55) can be written in a more compact form,

$$\Psi(Q_1, \ldots, Q_p, t) = \sum_J A_J \Phi_J, \tag{56}$$

with the composite index $J = (j_1, \ldots, j_p)$ and

$$A_J = A_{j_1 \ldots j_p}(t), \tag{57}$$

$$\Phi_J = \prod_{\kappa=1}^{p} \varphi_{j_\kappa}^{(\kappa)}(Q_\kappa, t). \tag{58}$$

As before, the Dirac-Frenkel variational principle Eq. (51) is applied to solve the time-dependent Schrödinger equation. This gives the equations of motion for the expansion coefficients as well as for the SPFs. The following constraints are applied on the SPFs,

$$\langle \varphi_j^{(\kappa)}(0) | \varphi_l^{(\kappa)}(0) \rangle = \delta_{jl} \tag{59}$$

$$\langle \varphi_j^{(\kappa)}(t) | \dot{\varphi}_l^{(\kappa)}(t) \rangle = -i \langle \varphi_j^{(\kappa)}(t) | \hat{g}^{(\kappa)} | \varphi_l^{(\kappa)}(t) \rangle. \tag{60}$$

The arbitrary, but Hermitian constraint operator $\hat{g}(t)$, is needed to uniquely define the equations of motion. It does not affect the resulting wave function, but the computational effort. The optimal choice of the constraints also depends on the integration scheme for the propagation, for example $\hat{g}^{(\kappa)} = 0$ is used when the efficient constant mean-field integrator, cf. Sec. (2.3.3), is applied. Otherwise, $\hat{g}^{(\kappa)} = h^{(\kappa)}$ is used in the Heidelberg MCTDH program.[106],[107] The Eqs. (59) and (60) also ensure that the SPFs are orthonormal at all times.

In the following, the working equations of motion are derived in detail. For this purpose, the definition of some of the below quantities are helpful. First of all, the single-hole function is defined as

$$\Psi_l^{(\kappa)} = \sum_{j_1} \cdots \sum_{j_{\kappa-1}} \sum_{j_{\kappa+1}} \cdots \sum_{j_p} A_{j_1 \ldots j_{\kappa-1} l j_{\kappa+1} \ldots j_p} \varphi_{j_1}^{(1)} \cdots \varphi_{j_{\kappa-1}}^{(\kappa-1)} \varphi_{j_{\kappa+1}}^{(\kappa+1)} \cdots \varphi_{j_p}^{(p)}, \tag{61}$$

where the κth particle has been removed which leaves the hole l. With that we can further define the mean fields, i.e., the energy expectation value, by integrating over all particles except κ,

$$\langle H \rangle_{jl}^{(\kappa)} = \langle \Psi_j^{(\kappa)} | H | \Psi_l^{(\kappa)} \rangle, \tag{62}$$

and density matrices,

$$\rho_{jl}^{(\kappa)} = \langle \Psi_j^{(\kappa)} | \Psi_l^{(\kappa)} \rangle, \tag{63}$$

of which the eigenfunctions represent the so-called *natural orbitals*. Moreover, the projector on the space spanned by the SPFs for the kth DOF is defined as

$$\mathbf{P}^{(\kappa)} = \sum_{j=1}^{n_\kappa} |\varphi_j^{(\kappa)}\rangle \langle \varphi_j^{(\kappa)}|. \tag{64}$$

The notation of the single-hole function Eq. (61) and the short-hand notation of the SPF product Eq. (58) can be used to rewrite the parts that are needed for applying the variational principle

Eq. (51), which are the following,

$$\Psi = \sum_J A_J \Phi_J = \sum_{j_\kappa=1}^{n_\kappa} \varphi_{j_\kappa}^{(\kappa)} \Psi_{j_\kappa}^{(\kappa)}, \tag{65}$$

$$\dot{\Psi} = \sum_J \dot{A}_J \Phi_J + \sum_{\kappa=1}^{p} \sum_{j_\kappa=1}^{n_\kappa} \dot{\varphi}_{j_\kappa}^{(\kappa)} \Psi_{j_\kappa}^{(\kappa)}, \tag{66}$$

$$\delta\Psi/\delta A_J = \Phi_J, \tag{67}$$

$$\delta\Psi/\delta \varphi_{j_\kappa}^{(\kappa)} = \Psi_{j_\kappa}^{(\kappa)}. \tag{68}$$

For variations with respect to the coefficients Eq. (67), the Dirac-Frenkel variational principle Eq. (51) yields

$$0 = \langle \delta\Psi | \hat{H} | \Psi \rangle - i \langle \delta\Psi | \dot{\Psi} \rangle \tag{69}$$

$$= \langle \Phi_J | \hat{H} | \Psi \rangle - i \langle \Phi_J | \dot{\Psi} \rangle. \tag{70}$$

Using Eq. (66) as well as $\hat{g}^{(\kappa)} = 0$ for the constraint Eq. (60), we obtain

$$0 = \langle \Phi_J | \hat{H} | \Psi \rangle - i \langle \Phi_J | \sum_L \dot{A}_L | \Phi_L \rangle, \tag{71}$$

and hence, together with Eq. (65)

$$i\dot{A}_J = \langle \Phi_J | \hat{H} | \Psi \rangle \tag{72}$$

$$= \sum_L \langle \Phi_J | \hat{H} | \Phi_L \rangle A_L. \tag{73}$$

For the variation with respect to the SPFs Eq. (68), we get

$$0 = \langle \delta\Psi | \hat{H} | \Psi \rangle - i \langle \delta\Psi | \dot{\Psi} \rangle \tag{74}$$

$$= \langle \Psi_{j_\kappa}^{(\kappa)} | \hat{H} | \Psi \rangle - i \langle \Psi_{j_\kappa}^{(\kappa)} | \dot{\Psi} \rangle \tag{75}$$

$$= \underbrace{\langle \Psi_{j_\kappa}^{(\kappa)} | \hat{H} | \Psi \rangle}_{I} - \underbrace{i \sum_L \langle \Psi_{j_\kappa}^{(\kappa)} | \Phi_L \rangle \dot{A}_L}_{II} - \underbrace{i \sum_{\tilde{\kappa}=1}^{p} \sum_{l_{\tilde{\kappa}}=1}^{n_{\tilde{\kappa}}} \langle \Psi_{j_\kappa}^{(\kappa)} | \dot{\varphi}_{l_{\tilde{\kappa}}}^{(\tilde{\kappa})} \Psi_{l_{\tilde{\kappa}}}^{(\tilde{\kappa})} \rangle}_{III}, \tag{76}$$

where Eq. (66) has been inserted into Eq. (75). The three single terms of Eq. (76) can be rewritten

as follows,

$$I. \quad \langle \Psi_{j_\kappa}^{(\kappa)} | \hat{H} | \Psi \rangle = \sum_{l_\kappa=1}^{n_\kappa} \langle \Psi_{j_\kappa}^{(\kappa)} | \hat{H} | \varphi_{l_\kappa}^{(\kappa)} \Psi_{l_\kappa}^{(\kappa)} \rangle \quad \text{with Eq. (65), (62)} \tag{77}$$

$$= \sum_{l_\kappa=1}^{n_\kappa} \langle \hat{H} \rangle_{j_\kappa l_\kappa}^{(\kappa)} | \varphi_{l_\kappa}^{(\kappa)} \rangle, \tag{78}$$

$$II. \quad i \sum_L \langle \Psi_{j_\kappa}^{(\kappa)} | \Phi_L \rangle \dot{A}_L = \sum_L \langle \Psi_{j_\kappa}^{(\kappa)} | \Phi_L \rangle \langle \Phi_L | \hat{H} | \Psi \rangle \quad \text{with Eq. (72), (58), (61), (59)} \tag{79}$$

$$= \sum_{l_1 \dots l_p} A_{j_1,\dots,j_\kappa,\dots,j_p} | \varphi_{l_\kappa}^{(\kappa)} \rangle \prod_{\tilde{\kappa}=1}^{p} \langle \varphi_{l_{\tilde{\kappa}}}^{(\tilde{\kappa})} | \hat{H} | \Psi \rangle \tag{80}$$

$$\times \delta_{j_1 l_1} \dots \delta_{j_{\kappa-1} l_{\kappa-1}} \delta_{j_{\kappa+1} l_{\kappa+1}} \dots \delta_{j_p l_p} \tag{81}$$

$$= \sum_{l_\kappa} | \varphi_{l_\kappa}^{(\kappa)} \rangle \langle \varphi_{l_\kappa}^{(\kappa)} | \langle \Psi_{j_\kappa}^{(\kappa)} | \hat{H} | \Psi \rangle \quad \text{with Eq. (64), (65), (62)} \tag{82}$$

$$= \mathbf{P}^{(\kappa)} \sum_{l_\kappa=1}^{n_\kappa} \langle \hat{H} \rangle_{j_\kappa l_\kappa}^{(\kappa)} | \varphi_{l_\kappa}^{(\kappa)} \rangle, \tag{83}$$

$$III. \quad i \sum_{\tilde{\kappa}=1}^{p} \sum_{l_{\tilde{\kappa}}=1}^{n_{\tilde{\kappa}}} \langle \Psi_{j_\kappa}^{(\kappa)} | \dot{\varphi}_{l_{\tilde{\kappa}}}^{(\tilde{\kappa})} \Psi_{l_{\tilde{\kappa}}}^{(\tilde{\kappa})} \rangle = i \sum_{l_\kappa=1}^{n_\kappa} \rho_{j_\kappa, l_\kappa}^{(\kappa)} | \dot{\varphi}_{l_\kappa}^{(\kappa)} \rangle \quad \text{with Eq. (63).} \tag{84}$$

Hence, Eq. (76) can be restructured as,

$$i \sum_{l_\kappa=1}^{n_\kappa} \rho_{j_\kappa, l_\kappa}^{(\kappa)} | \dot{\varphi}_{l_\kappa}^{(\kappa)} \rangle = (1 - \mathbf{P}^{(\kappa)}) \sum_{l_\kappa=1}^{n_\kappa} \langle \hat{H} \rangle_{j_\kappa l_\kappa}^{(\kappa)} | \varphi_{l_\kappa}^{(\kappa)} \rangle. \tag{85}$$

As a consequence, the Eqs. (73) and (85) turn out as the MCTDH working equations of motion, that look after rearranging as follows,

$$i \dot{A}_J = \sum_L \langle \Phi_J | \hat{H} | \Phi_L \rangle A_L, \tag{86}$$

$$i | \dot{\varphi}_{l_\kappa}^{(\kappa)} \rangle = (1 - \mathbf{P}^{(\kappa)}) \Big(\rho_{j_\kappa, l_\kappa}^{(\kappa)} \Big)^{(-1)} \langle \hat{H} \rangle_{j_\kappa l_\kappa}^{(\kappa)} | \varphi_{l_\kappa}^{(\kappa)} \rangle. \tag{87}$$

For all possible configurations J and all particles κ, Eqs. (86) and (87) present a system of coupled nonlinear first order differential equations. When building the inverse of the density matrix on the right side in Eq. (87), singularities can be avoided by using a regularized form[106]

$$\rho_{\text{reg}}^{(\kappa)} = \rho^{(\kappa)} + \varepsilon \exp\left(-\rho^{(\kappa)} / \varepsilon\right), \tag{88}$$

with very small $\varepsilon \approx 10^{-8}$.

The advantage of the MCTDH method lies in the flexible wave function ansatz that allows for compactness, such that a small number of functions already yields good qualitative results. In contrast to the beforehand presented methods, with MCTDH it is possible to include different types of correlations. Thus, the accuracy increases in comparison to TDH, while at the same time MCTDH is of less effort than the standard method.

2.2.4 Fermionic wave functions

It should be noticed that the MCTDH method does *not* imply the antisymmetry of fermions per se. The general solution of the Schrödinger equation for indistinguishable particles fulfilling the Pauli exclusion principle is given in form of a Slater determinant (SD),

$$\Psi^{(\mathrm{SD})} = \sqrt{\frac{1}{N!}} \begin{vmatrix} \varphi_1(r_1,\sigma_1) & \varphi_2(r_1,\sigma_1) & \cdots & \varphi_N(r_1,\sigma_1) \\ \varphi_1(r_2,\sigma_2) & \varphi_2(r_2,\sigma_2) & \cdots & \varphi_N(r_2,\sigma_2) \\ \vdots & \vdots & \ddots & \vdots \\ \varphi_1(r_N,\sigma_N) & \varphi_2(r_N,\sigma_N) & \cdots & \varphi_N(r_N,\sigma_N) \end{vmatrix},$$

where the spin orbital functions $\varphi_j(r_i,\sigma_i) = \psi_j(r_i)\theta_j(\sigma_i)$ are products of molecular orbitals ψ_j and spin functions θ_j. The molecular orbital function itself can be described by a linear combination of orthonormal basis functions $|\psi_j\rangle = \sum_\nu c_{\nu j}|\chi_\nu\rangle$.

In the studies presented in this thesis, the system is assumed to be initially in a triplet state $|s,m\rangle$ for which the spin quantum number $s = 1$ and the magnetic quantum number $m = \{-1,0,1\}$ apply. These quantum numbers give the spin triplet states $|1,1\rangle = \uparrow\uparrow$, $|1,0\rangle = \frac{1}{\sqrt{2}}(\uparrow\downarrow + \downarrow\uparrow)$ and $|1,-1\rangle = \downarrow\downarrow$. As the triplet states are symmetric the spatial part is required to be antisymmetric. This is to maintain the antisymmetry of the total wave function being the product of spin and orbital function. It is taken into account by imposing the condition

$$A_{j_1,\ldots,j_\kappa,\ldots,j_{\kappa'},\ldots,j_p} = -A_{j_1,\ldots,j_{\kappa'},\ldots,j_\kappa,\ldots,j_p} \tag{89}$$

for particle exchange on the A-vector of the MCTDH wave function Eq. (55).

2.3 Computational methods

The MCTDH Heidelberg code[106], [107] has been used for computations. It utilizes grid-based computational methods which store quantities like the wave function and operators in tensor-form. The following section shall give an overview over these methods.

2.3.1 Discrete variable representation

Solving the MCTDH equations of motion, Eq. (86) and (87), needs evaluation of the Hamilton matrix elements $\langle\Phi_J|\hat{H}|\Phi_L\rangle$ as well as the mean fields $\langle H\rangle_{jl}^{(\kappa)}$ as defined in Eq. (62). This means to calculate multidimensional integrals. To cope with this task, the MCTDH Heidelberg program utilizes time-independent bases with orthonormal functions in a *discrete variable representation*, or short DVRs.[108]–[110]

Consider the DVR basis set $\left\{\chi^{(\nu)}(q_\nu)\right\}$ defined for coordinate q_ν. The matrix representation of the position operator $\hat{q}_\nu$ in this basis is diagonal, i.e.,

$$\langle\chi_i^{(\nu)}|\hat{q}_\nu|\chi_j^{(\nu)}\rangle = \tilde{q}_j^{(\nu)}\delta_{ij}, \tag{90}$$

for which the matrix element can be evaluated analytically and the set of position operator eigenvalues $\{\tilde{q}^{(\nu)}\}$ define a *grid of points* in the specific DVR basis. These points build the basis on which the wave function will be represented and the number of grid points corresponds to the number of DVR basis functions. Different types of DVRs have been developed for standard wave packet propagations, e.g., harmonic oscillator DVRs that use harmonic oscillator eigenfunctions for vibrational motion, Legendre DVRs for rotations, or exponential and sine DVRs that uses the particle-in-a-box eigenfunctions to describe free moving particles.

The integrals in Eqs. (86) and (87) are still in the basis of the SPFs of the MCTDH wave function Eq. (55). However, the SPFs can be expanded in the DVRs, which results in the so-called *primitive basis functions*,

$$\varphi_j^{(\kappa)}(Q_\kappa) = \sum_{\mathrm{k}=1}^{N_\kappa} a_{\mathrm{k}j}^{(\kappa)}\chi_{\mathrm{k}}^{(\kappa)}(Q_\kappa). \tag{91}$$

Note that N_κ is the number of DVRs and different from the number of SPF n_κ as defined in Eq. (55). The DVRs are usually one-dimensional, but the SPFs might be of higher dimension due to possible mode combinations (cf. Sec. 2.2.3). For a particle's combined coordinate $Q_1 = (q_1, q_2)$, the multidimensional SPFs can be expressed by products of primitive basis functions,

$$\varphi_j^{(1)}(Q_1) = \sum_{\mathrm{k}_1=1}^{N_1}\sum_{\mathrm{k}_2=1}^{N_2} a_{\mathrm{k}_1\mathrm{k}_2 j}^{(1)}\chi_{\mathrm{k}_1}^{(1)}(q_1)\chi_{\mathrm{k}_2}^{(2)}(q_2). \tag{92}$$

The transformation of the SPFs yields the full primitive product grid of size $\prod_{\kappa=1}^{f} N_\kappa$. To reduce the dimensionality of the integral in Eq. (86), the Hamiltonian is expressed as a sum of products of single-particle operators, which depend on the p particle coordinates,

$$H(Q_1,\ldots,Q_p) = \sum_{r=1}^{n_s} c_r h_r^{(1)}(Q_1)\cdots h_r^{(p)}(Q_p). \tag{93}$$

With this, the multidimensional integral can be converted into

$$\langle \Phi_J | \hat{H} | \Phi_L \rangle = \langle \varphi_{j_1}^{(1)} \cdots \varphi_{j_p}^{(p)} | \hat{H} | \varphi_{l_1}^{(1)} \cdots \varphi_{l_p}^{(p)} \rangle \tag{94}$$

$$= \sum_{r=1}^{n_s} c_r \langle \varphi_{j_1}^{(1)} | h_r^{(1)} | \varphi_{l_1}^{(1)} \rangle \cdots \langle \varphi_{j_p}^{(p)} | h_r^{(p)} | \varphi_{l_p}^{(p)} \rangle. \tag{95}$$

Together with the primitive basis functions Eq. (91) we are now left with the product of integrals of significantly lower dimension d for each particle κ. The integrals are now evaluated on the primitive grid of size N_κ^d.

The kinetic energy operator and other single-particle Hamiltonians can be brought into product form of Eq. (93). This is not possible for potential energy functions that contain inter-particle correlation, like for example the Coulomb interaction between two particles. To bring those functions into the desired product form, the *POTFIT* method has been developed as introduced in the following section.

2.3.2 Potential fitting methods (POTFIT and multigrid POTFIT)

The MCTDH method requires the Hamilton operator to be of product form (Eq. (93)), which is not trivial for non-separable potentials. The multi-dimensional exact potential, which might be given as a list of points or an analytical function, must be defined on the whole product grid

$$V(\tilde{q}_{i_1}^{(1)}, \ldots, \tilde{q}_{i_f}^{(f)}) \equiv V_{i_1 \ldots i_f}, \tag{96}$$

where $\tilde{q}_{i_\kappa}^{(\kappa)}$ is the i_κth grid point of the one-dimensional grid that represents the κth DOF with $1 \leq i_\kappa \leq N_\kappa$. Then, the non-separable potential can still be brought into product form by its expansion in an orthonormal product basis, that is complete over the grid points. For p particles with combined modes $\tilde{Q}_\kappa$ the approximated potential then looks as follows,

$$V^{\text{app}}(\tilde{Q}_{i_1}^{(1)}, \ldots, \tilde{Q}_{i_p}^{(p)}) = \sum_{j_1=1}^{m_1} \cdots \sum_{j_p=1}^{m_p} C_{j_1,\ldots,j_p} v_{j_1}^{(1)}(\tilde{Q}_{i_1}^{(1)}) \ldots v_{j_p}^{(p)}(\tilde{Q}_{i_p}^{(p)}), \tag{97}$$

with the expansion coefficients $C_{j_1,\ldots,j_p}$ and expansion orders m_κ. The latter must be large enough for an accurate expansion, but at the same time as small as possible to minimize the computational effort. If the expansion orders $\{m_\kappa\}$ are set equal to the number of grid points $\{N_\kappa\}$, then the approximated potential is equal to the exact one at the grid points. The basis functions $v_{j_\kappa}^{(\kappa)}$ are called single-particle potentials (SPPs) and are of the kth particle's dimension. The expansion coefficients are accordingly the overlaps between the exact potential and the SPPs on all grid points,

$$C_{j_1,\ldots,j_p} = \sum_{j_1=1}^{N_1} \cdots \sum_{j_p=1}^{N_p} V_{i_1 \ldots i_p} v_{j_1}^{(1)}(\tilde{Q}_{i_1}^{(1)}) \ldots v_{j_p}^{(p)}(\tilde{Q}_{i_p}^{(p)}). \tag{98}$$

The one-particle potential density matrix elements are defined as

$$\rho_{\mathrm{kk'}}^{(\kappa)} := \sum_{I^\kappa} V_{I_{\mathrm{k}}^\kappa} V_{I_{\mathrm{k'}}^\kappa} \tag{99}$$

with the sum over all grid points for all DOFs except the κth one, whose grid points are fixed at k and k$'$, or more precisely, with the composite index $I^\kappa = (i_1, \ldots, i_{\kappa-1}, i_{\kappa+1}, \ldots, i_f)$ and $I^\kappa_k = (i_1, \ldots, i_{\kappa-1}, \mathrm{k}, i_{\kappa+1}, \ldots, i_f)$. After diagonalization of ρ, whose elements are defined in Eq. (99), the resulting eigenvectors are taken as the SPPs. The eigenvalues indicate the relevance of the eigenvectors, such that the series can be truncated after small enough eigenvalues.

The coefficients are determined by error minimization between the exact and approximated potential, i.e., minimizing

$$\Delta^2 = \sum_I (V_I - V_I^{\mathrm{app}})^2 w_I^2, \tag{100}$$

with the composite index I running over the full product grid. With the weight functions w_I it is possible to regulate at which points the minimization should be performed how accurately.

To allow for further reduction of the numerical effort without affecting the accuracy of the MCTDH calculations, so-called *contracted expansion coefficients* are introduced,

$$D_{j_1 \ldots j_{\kappa-1} j_{\kappa+1} \ldots j_p} = \sum_{j_\kappa=1}^{m_\kappa} C_{j_1, \ldots, j_p} v^{(\kappa)}_{j_\kappa} \tag{101}$$

which reduce the number of the expansion terms in Eq. (97) by a factor m_κ. Contractions should best be done for the particle κ with the largest expansion order m_κ.

The standard POTFIT consumes large memory for expressing and storing a quantity on the full grid. This limits the grid size that it can handle numerically, that is typically up to 10^9 grid points or a six-dimensional system. Alternatively, the *multigrid POTFIT* (MGPF) method[111] can treat systems up to 12 dimensions. It is a POTFIT-based approach that manages to significantly decrease computation times for bringing the potential into product form, while still being of equal quality as POTFIT. MGPF circumvents the dimensionality issues of POTFIT by avoiding computation on the full grid and, instead, using a hierarchy of grids. The full primitive product grid of size $\prod_{\kappa=1}^f N_\kappa$, for which the numerical results are converged up to a desired accuracy, is called here the *fine* grid with the composite grid point index $\tilde{I}$. For each DOF a subset of the fine grid is defined, called *coarse grid* with index I. MGPF performs a series of POTFIT calculations, in which a particular mode lies on the fine grid, whereas the rest lie on the coarse grid. This results in a series of stepwise minimizations, one for each DOF,

$$\sum_{I^\kappa} \sum_{\tilde{i}_\kappa} (V_{I^\kappa_{\tilde{i}_\kappa}} - V^{\mathrm{app}}_{I^\kappa_{\tilde{i}_\kappa}})^2 = \text{minimum}, \quad \text{for } \kappa = 1, \ldots, f, \tag{102}$$

where $V^{\mathrm{app}}_{I^\kappa_{\tilde{i}_\kappa}}$ is the approximated potential in which the coarse grid SPPs for the kth DOF have been replaced by the corresponding SPPs on the fine one.

The MGPF method is by nature less accurate than standard POTFIT, on the other hand it allows to treat systems with significantly larger numbers of DOFs. For us, it was only recently possible to treat the two-particle system in a two-dimensional continuum, i.e., a four-dimensional grid of 140 grid point per dimension, as presented in Sec. 3 or [A.3].

2.3.3 Integration scheme used for propagation

The *constant mean-field* (CMF) integration scheme is the algorithm which is used for solving the MCTDH equations of motion for the coefficients Eq. (86) and the SPFs Eq. (87), and consequently for propagating the wave function Eq. (55).

In principle, the integration must be done for very small consecutive time steps, as the MCTDH coefficients and SPFs are strongly coupled. The CMF algorithm uses the fact that the Hamiltonian matrix elements $\langle\Phi_J|\hat{H}|\Phi_L\rangle$ and the product of inverse density and mean-field matrices $(\rho^{(\kappa)}_{j_\kappa,l_\kappa})^{(-1)}\langle\hat{H}\rangle^{(\kappa)}_{j_\kappa l_\kappa}$ change much slower in time than the MCTDH coefficients and SPFs. Hence, the former two quantities can be held constant for some time during propagation, and do not have to be updated as often as the coefficients and SPFs. Moreover, during the constant mean field time, the equations of motion for the coefficients and SPFs are uncoupled from each other, which facilitates their integration.

2.3.4 Relaxation of the wave function

For the propagation of the wave function an initial state needs to be provided that constitutes the starting point $|\Psi(0)\rangle$. Oftentimes, the ground state is used, i.e., the eigenfunction of the system's Hamiltonian with lowest energy. With the method of *energy relaxation* the ground state eigenfunction can be generated by propagating a guess function in negative imaginary time $t = -i\tau$,[112]

$$|\Psi_{\text{relax}}(\tau)\rangle = N(\tau)e^{-\hat{H}\tau}|\Psi_{\text{guess}}(0)\rangle. \tag{103}$$

The guess function can be expanded in the eigenfunctions of the time-independent Hamiltonian $\hat{H}$ by making use of the completeness of the basis and inserting the unity $\mathbb{1} = \sum_j |\phi_j\rangle\langle\phi_j|$,

$$|\Psi_{\text{relax}}(\tau)\rangle = N(\tau)\sum_j a_j e^{-E_j\tau}|\phi_j\rangle, \tag{104}$$

with coefficients $a_j = \langle\phi_j|\Psi_{\text{guess}}(0)\rangle$ and eigenvalues E_j of $\hat{H}$. After each time step Eq. (104) must be renormalized by the factor $N(\tau) = \|e^{-\hat{H}\tau}|\Psi_{\text{guess}}(0)\rangle\|^{-1}$. The guess wave packet is usually a simple product of SPFs, which can be given for example in form of Gaussian functions. It is also possible to use eigenfunctions obtained through diagonalization of single-particle Hamiltonians. The combination of both, mathematical functions and operator eigenfunctions into a guess function, is also possible.

As decay times are inverse proportional to the energies, the ground state $|\phi_0\rangle$ relaxes the slowest, since it is of lowest energy $E_0 < E_j$ for $j = 1, 2, \ldots$. For long enough propagation times the wave function $\Psi_{\text{relax}}(\tau)$ hence converges to the ground state. By removing the ground state from the Hilbert space, through keeping $\Psi_{\text{relax}}(\tau)$ orthogonal to ϕ_0, the first excited state can be computed by the same principle of energy relaxation, and so on for higher states.

There is a more efficient way to compute the eigenstates, which is called *improved relaxation*. By making use of the CMF integration scheme when propagating the equations of motion, Eq. (86)

and (87), the A-coefficients can be treated as decoupled from the SPFs. Rather than by energy relaxation, the A-vector can then be determined by diagonalization of the matrix which is built of the elements $\langle\Phi_J|\hat{H}|\Phi_L\rangle$ in Eq. (86). Moreover, the SPFs are obtained through energy relaxation as before.

2.3.5 Complex absorbing potentials

There is one drawback when using grid-based methods for electron dynamics calculations, that is, any free moving wave packet part will be unnaturally reflected at the grid ends, or reenters from the other side of the grid for periodic boundary conditions. In the case of our studies, the continuum electron that was ejected due to ICD returns towards the QDs where it can interact again with the other electron that is still bound in the left dot. This needs to be circumvented.

The straightforward solution would be making the grids very large to obtain long enough observation times, but of course this is not in favor of memory consumption. Another answer to this problem is the use of *complex absorbing potentials* (CAP).[97],[113] The CAP as part of the Hamiltonian annihilates the free wave packet before it reaches the ends of the grids. CAPs of the following form have been used,

$$\hat{W}^{\pm}_{q_\kappa} = -i\,\eta_{\mathrm{CAP}}|q_\kappa - q_{\kappa,\pm}|^n\Theta\big(\pm(q_\kappa - q_\pm)\big). \tag{105}$$

For each DOF q_κ the operator $\hat{W}^{\pm}_{q_\kappa}$ defines the CAP of nth order that is placed right ("+") or left ("−") from the bound system and starts at $q_{\kappa,+}$ or $q_{\kappa,-}$, respectively. The Heaviside step function keeps the inner region between $q_{\kappa,-}$ and $q_{\kappa,+}$ CAP-free. The CAP strength η_{CAP} must be optimized to maximize absorption and at the same time minimize reflections from the CAP. Furthermore, it should be long enough such that the wave packet is sufficiently removed before it can reach the grid's end.

As a consequence, using CAPs allows to compute on much smaller grids, for which otherwise reflected particles would disturb the process within the localized regions after only short propagation times. However, the CAP as a complex operator also introduces a non-Hermitian potential term to the Hamiltonian. The total Hamiltonian can be written as,

$$\hat{H} = \hat{H}' - i\hat{H}'' \quad \text{and} \quad \hat{H}^\dagger = \hat{H}' + i\hat{H}'', \tag{106}$$

and the Schrödinger equation is,

$$|\dot{\Psi}(t)\rangle = -i\hat{H}|\Psi(t)\rangle \quad \text{and} \quad \langle\dot{\Psi}(t)| = i\langle\Psi(t)|\hat{H}^\dagger. \tag{107}$$

Then, by calculating the time-derivative of the wave function norm,

$$\frac{\partial}{\partial t}\langle\Psi|\Psi\rangle = \langle\dot{\Psi}|\Psi\rangle + \langle\Psi|\dot{\Psi}\rangle \tag{108}$$

$$= i\langle\Psi|\hat{H}^\dagger|\Psi\rangle - i\langle\Psi|\hat{H}|\Psi\rangle \tag{109}$$

$$= -2\langle\Psi|\hat{H}''|\Psi\rangle < 0, \tag{110}$$

reveals that the norm decreases when a CAP is present. Usually, for Hermitian systems the wave function norm $\langle\Psi(t)|\Psi(t)\rangle$ integrated over the whole coordinate space equals unity at all times. Here however, the CAP annihilates free wave packets which afterwards are not part of the system anymore. This feature of the CAPs must be kept in mind when analyzing state populations.

3 Results & Conclusions

In this thesis the inter-Coulombic decay process was studied in pairs of singly-charged quantum dots, where one QD gets excited and relaxes by transferring energy to the other one, which in consequence is ionized. The ICD process was predicted in many calculations for atomic and molecular systems and recently for charged QDs. Various experimental observations have been made already for atoms and molecules, however none for QDs so far.

The goal of this thesis was to perform electron dynamics calculations of the QD-ICD with particular regard to the experimental feasibility, and to check here different possibilities for laser control. The three main control options are the focus, the intensity and the polarization of the exciting laser. In all works covered by this thesis[A.1]-[A.3] the electron dynamics calculations for the two same-spin electrons were performed in terms of a highly-accurate wave function approach, i.e., the multiconfiguration time-dependent Hartree method. Furthermore, two different QD geometries have been studied, which were QDs in a nanowire with a single continuum dimension,[A.1],[A.2] and self-assembled QDs of lateral arrangement connected to a two-dimensional continuum.[A.3] Both are well-characterized QD arrangements and are promising for identifying ICD in a future experiment.

In [A.1] and [A.2] the calculations were performed for a one-dimensional Gaussian binding model potential for which the QD pair expands over approximately 100 nm. The computations were done on two different grids: firstly, a short grid of ca. 1.1 μm length with 140 points and with absorbing boundary conditions, and secondly, a long grid of ca. 7.6 μm length and with 980 points. The long grid is hard-walled as ICD can be observed for reasonable durations before backscattered electrons start to penetrate again the QDs at the grid center.

The laser, which has an initiating and a controlling function, shall optimally excite the ground state into the resonance state which afterwards decays via ICD. Hence, competing excitation processes that hinder the QDs to undergo ICD shall be minimized. With regard to this, it was studied how direct ionization and multi-photon processes depend on the focus and intensity of the laser. For this purpose, the populations of the different two-electron states were determined as a function of time.[A.2] Fig. 6 shows all possible excitation paths from the ground state into the resonance or the different continuum states, as well as the decay by ICD. It was found that after an infrared π-pulse excitation with a resonant and linearly polarized laser 70% of the ground state L_0R_0 is excited into the resonance state L_1R_0, if the laser is applied on the whole system.[A.1] The remaining population is excited by multi-photon processes into the L_1C (continuum) states, which includes direct ionization of the right dot ($R_0 \rightarrow C$). On the other hand, when the laser is focused on the left dot the resonance state is populated by 95%, thus the almost exclusive excitation pathway is $L_0R_0 \rightarrow L_1R_0$ and other excitation processes are mostly ruled out.[A.2] This is also shown in the rate for direct ionization, which is five times higher when the laser is applied on both dots in comparison to being focused on the left dot only. Independent of the focus, contributions

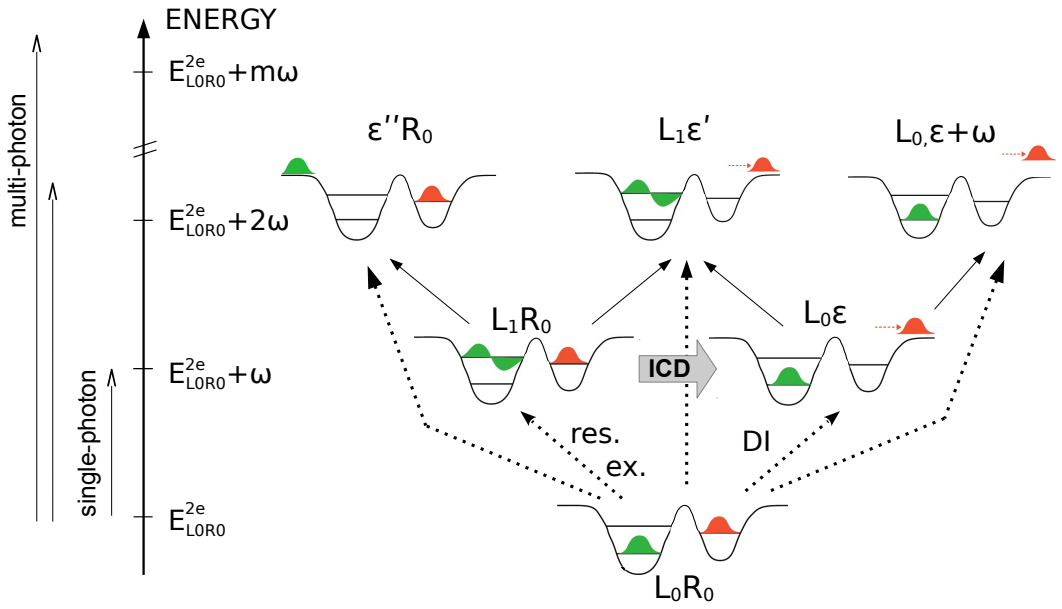

Figure 6: The light-induced ICD process in the two-electron QD pair with the ground state $|L_0R_0\rangle$ as the initial state here shown for a laser directed on both QDs. After resonant excitation (res. ex.) by a short laser pulse, the resonance state $|L_1R_0\rangle$ decays via ICD into a continuum state $|L_0\varepsilon\rangle$ of the same energy. Besides ICD, the direct ionization (DI) of the ground state by the laser is possible. During the excitation, states of higher energies $E^{2e}_{L_0R_0} + m\omega$ with $m > 1$ can be populated via multi-photon processes, either via direct m-photon excitation (dotted arrows) or m consecutive single-photon processes (short arrows). Reprint with permission from Haller et al. [A.2] (©2018 American Institute of Physics)

for ionization of the left dot ($L_0 \rightarrow L_1 \rightarrow C$) were found to be marginal for the π-pulse. These results coincide with what was found in earlier studies,[54] however here the excitation path of the electron can be followed in detail due to novel analyses techniques.

For increasing laser intensities the direct ionization of the left QD by means of multi-photon excitations becomes more and more relevant.[A.2] For example, 1% of the population that is initially in the L_0 level will be ionized after a left-focused π-pulse. This value rises to 51% for an also left-focused 5π-pulse, i.e., a pulse of the same length but an approximately five times higher intensity, that oscillates the population five times between ground and resonance state. For a 9π-pulse already 91% of the population in the left dot is ionized. As a consequence, the impact of ICD becomes negligible. After the pulse, for either laser focus and intensity, solely ICD can take place via $L_1R_0 \xrightarrow{(\mathrm{ICD})} L_0C$ as long as the resonance state population in non-zero. Hence, all other state populations stay constant.

The total ionization probability is a measure for all ionization pathways, i.e., ICD as well as direct ionizations including multi-photon excitations. The probability was calculated for a scan over different field strengths at constant pulse length (ca. 15 ps or 1/10 of the ICD time).[A.1],[A.2] The scan, as shown in Fig. 7, was used to determine the distinct field strengths which induce a

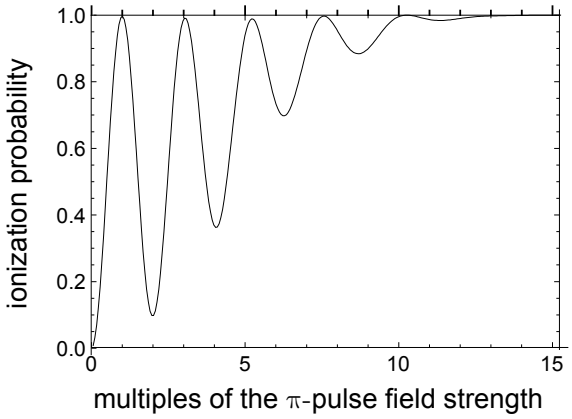

Figure 7: Total ionization probability for the QD-in-a-wire system scanned over the field strength of the exciting left-focused laser for constant pulse length. The field strength is given in units of the π-pulse field strength that induces exactly one population inversion between ground and resonance state. Figure adapted from [A.2].

certain number of Rabi cycles, i.e., population inversions from the ground to the resonance state and back during the lasing period. As a matter of fact, the ionization probability oscillates as well with varying field strength. The probability for ionization becomes one at field strengths of odd $n\pi$-pulses. It means that by the end of the pulse the laser has transferred the complete electronic density that is still within the dot region into the resonance state, which then eventually decays via ICD. The oscillation minima are found at those field strengths for which the electrons have been brought back to the ground state, and thus remain in the dots, when the pulse has finished, i.e., at even $n\pi$. For those field strengths ICD and direct ionizations are only possible during the short lasing period. Since direct ionization gains importance with increasing field strength, the minima of the total ionization probability increase as well.

The Rabi oscillations can directly be observed in the population of the resonance state, where an $n\pi$-pulse induces $n/2$ Rabi cycles as shown in Fig. 8 for the focused laser. Generally, for odd $n\pi$-pulses (a) the electron density within the QDs is in the resonance state by the end of the pulse and decays via ICD afterwards. Otherwise, even $n\pi$-pulses (b) induce completed Rabi cycles, such that the dot population is in the ground state at the end of the pulse, and the resonance is completely depopulated preventing further ICD. Since the laser focus strongly influences the impact of direct ionization, only 1.5 Rabi cycles were visible for an unfocused laser (not shown in Fig. 8),[A.1] whereas for a laser focused on the left dot up to 6 Rabi cycles were observed.[A.2]

A number of several other analyses were performed. Besides explicitly solving the time-dependent Schrödinger equation in the space-resolved fashion of MCTDH calculations, an alternative, but more simplistic, state-resolved ansatz has been applied. This additional method was used to consolidate and interpret the results of the space-resolved method.[A.1],[A.2] The derivation, which was originally developed for the description of the resonant Auger decay in atoms,[114],[115] was adapted for the QD-ICD scenario.[A.1] In this ansatz, the total wave function is expanded

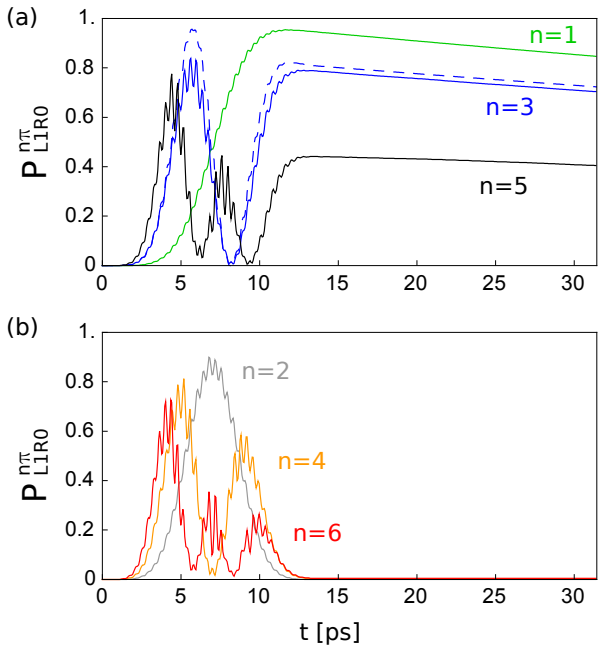

Figure 8: Resonance state populations for the nπ-laser pulse excitations for (a) n = 1, 3, 5 and (b) n = 2, 4, 6 with a focus on the left QD. The space-resolved calculations are performed on the long CAP-free grid (solid lines). A comparison is made to the state-resolved method for the 3π-pulse (dashed blue line). For the constant pulse length $t_{\mathrm{pulse}} = 14.1\,\mathrm{ps}$, the field strengths $\eta_{n\pi}$ are applied as obtained from the scan. Reprint with permission from Haller et al. [A.2] (©2018 American Institute of Physics)

in the orthonormal basis of the time-independent two-electron eigenstates, thus it is represented by a linear combination of the states with time-dependent coefficients. The latter contain the information on the state populations. For simplification, a restriction is made on the states that are allowed to be populated by excluding multi-photon excited states. This means that only the scenario for weak and left-focused lasers can be described with this ansatz. The calculations are significantly faster, but require an a priori calculation of all relevant energies and transition rates, thus they cannot replace the main MCTDH method.

Another analysis was done concerning the absorbing boundary conditions that showed to have an impact on the computations.[A.2] After the resonant excitation of the ground state the computations on the short grid with absorbing boundaries revealed an overall lower, thus physically wrong population of the resonance state. This was explained by the presence of the absorbing boundaries that may accelerate the direct photoionization of the electron in the right QD. By contrast, the computations on the long grid gave the physically correct description of the state populations, but require a compromise on computational effort and limitation of the propagation times until the dynamics is disturbed by backscattered electrons. In fact, the decay for the given example can only be observed for ca. 64 ps, that is about 1/3 of the ICD decay time. Despite the deviations in absolute values, the resonance state populations decrease with always the identical

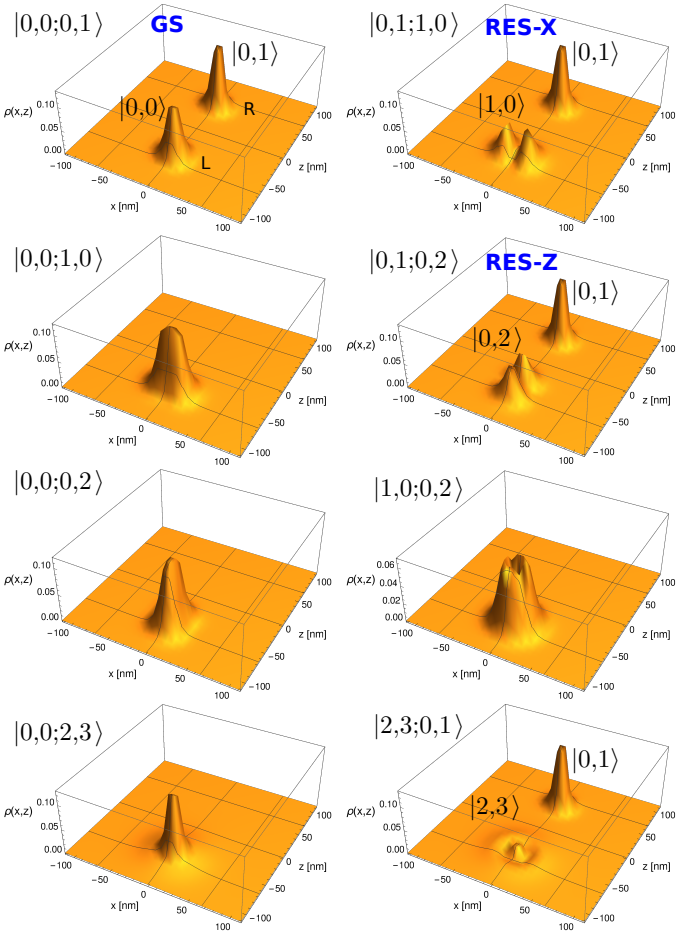

Figure 9: Electronic structure of two laterally arranged QDs represented by two-dimensional confining potentials. The figure shows the wave function densities of the two-electron states $|m_{x_1}, n_{z_1}; m_{x_2}, n_{z_2}\rangle$ in the triplet configuration. The ground state (GS) and the two degenerate resonance states in x (RES-X) and in z (RES-Z) are the relevant states for which ICD was studied. Figure adapted from [A.3].

ICD rate independent of the grids and boundaries. Therefore, if only the ICD rate is of interest, computing on the short grid provides sufficiently accurate results.

Turning to the third laser control option of the QD-ICD process, the laser polarization was studied with the aim to control the emission direction of the ICD electron.[A.3] Therefore, a second continuum direction was allowed by using a two-dimensional Gaussian binding model potential for the QD pair. It has three discrete levels in x ($m_x = 0, 1, 2$) and four in z, of which three lie in the left QD ($n_z = 0, 2, 3$) and one in the right dot ($n_z = 1$). They combine to the five different single-electron states $|m_x, n_z\rangle = \{|0,0\rangle, |0,1\rangle, |1,0\rangle, |0,2\rangle, |2,3\rangle\}$, from which one obtains eight two-electron states for uncoupled electrons in the triplet configuration, as depicted in Fig. 9.

In the interacting two-electron picture, each dimension reveals one resonance state that was found to decay via ICD. The process was initiated by a resonant π-pulse sampling different polarizations. The efficient preparation of the resonance states was, as in [A.2], achieved by a focused

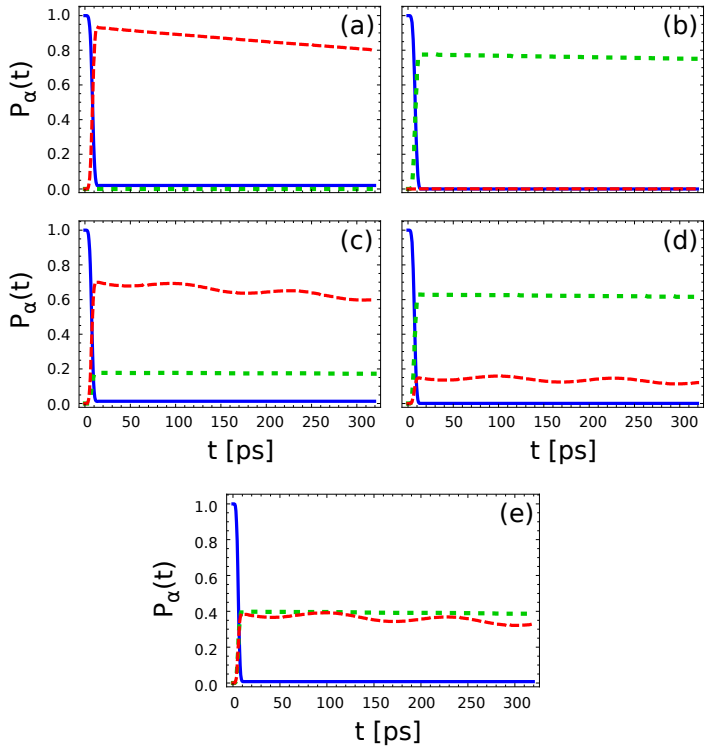

Figure 10: Time evolution of the population $P_\alpha(t)$ for the ground state (blue solid line) and resonance states in x (green dotted line) and z direction (red dashed line) for resonant π-pulse excitations. The upper row displays the case of linear polarization with $\varepsilon_x = 0.0$ and $\varepsilon_z = 1.0$ (a), and $\varepsilon_x = 1.0$ and $\varepsilon_z = 0.0$ (b) for the pulse length $t_{\text{pulse}}^{\text{linear}} = 16.6\,\text{ps}$. The middle row shows elliptical polarization with $\varepsilon_x = 0.5$ and $\varepsilon_z = 1.0$ (c), and $\varepsilon_x = 1.0$ and $\varepsilon_z = 0.5$ (d) with $t_{\text{pulse}}^{\text{elliptical}} = 14.8\,\text{ps}$. In (e) the system is excited by circularly polarized light with $\varepsilon_x = \varepsilon_z = 1.0$ and $t_{\text{pulse}}^{\text{circular}} = 11.6\,\text{ps}$. Reprint with permission from Haller et al. [A.3] (©2019 American Chemical Society)

laser directed on the left QD to minimize excitations by direct ionization. Fig. 10 shows the time-dependent populations under the excitations by differently polarized light with the ground state as initial configuration. Under linearly polarized light, either in z (a) or x (b), one of the resonances is populated, while the other stays unpopulated. When changing to elliptical polarization, (c) and (d), the other resonance state is admixed to the total population. For circular polarization (e) both resonances get equally populated. For excitations with non-linearly polarized light the decay of the z-resonance is overlaid with oscillations, cf. red line in Fig. 10 (c)-(e). The reason for this is the beating between the two resonances due to a small difference in the resonance energies. In general, the decay of the z-resonance is four times faster than that of the x-resonance. This is due to geometrical reasons, as the overlap of both electrons is larger for the z-resonance and hence energy transfer from the left to the right QD is more efficient.

In [A.3] it could be shown that the emission direction of the electron depends on the polarization of the exciting laser, cf. Fig. 11. As discussed before, linearly polarized light excites only one of

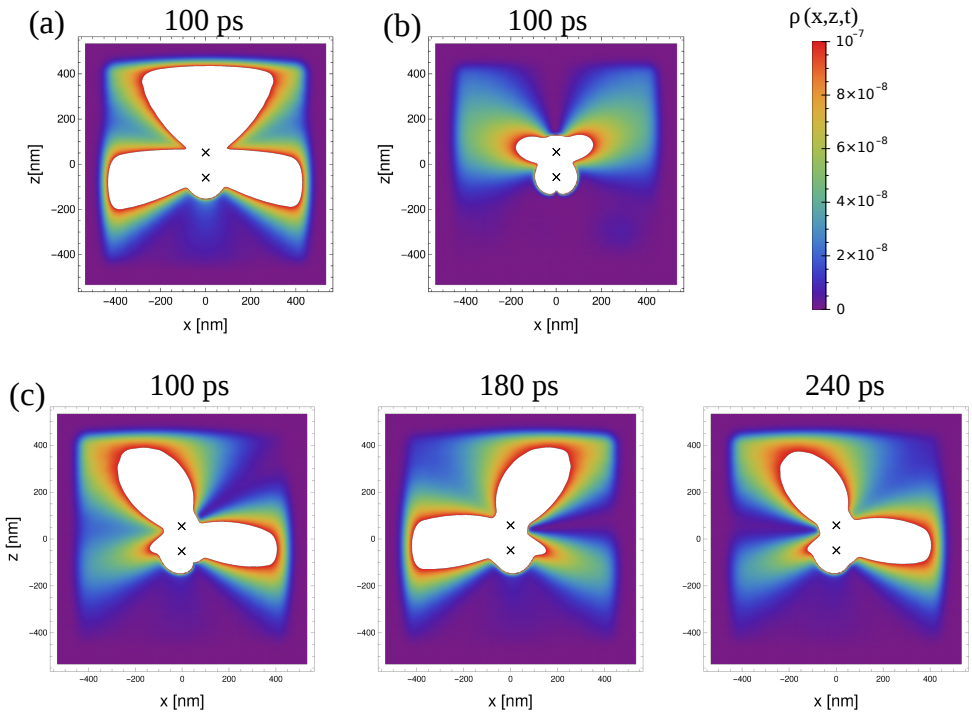

Figure 11: Electron wave function density for ICD in QDs with two-dimensional continuum. The decay is shown after exciting the ground state with linearly polarized light in z (a) and in x (b), and with circularly polarized light (c). The "$\times$" mark the centers of the QDs. Figure adapted from [A.3].

the resonance states. It was found that the decay of either resonance is uniform, that means the emission direction does not change over time, cf. Fig. 11 (a) and (b). For the decay of the z-resonance, (a), the electron in the right QD leaves particularly into $\pm x$ and $+z$. The negative z direction is avoided because of the Coulomb barrier that is formed by the electron in the left QD. As the density splits equally into positive and negative x a drift towards negative z can be observed, which means that momentum transfer from x to z is possible, which is here due to the non-separable Gaussian potential. Moreover, it was shown that the decay becomes 1.6 times slower if the electron is hindered to move into x, which was realized by applying infinitely high walls left and right from the dots in x direction.

For the uniform decay of the x-resonance, (b), most density leaves into x with equal distribution into positive and negative direction and with drift towards the positive z direction. Again, the barrier that is formed by the electron in the left dot does not allow motion in negative z.

The density for the decay of the mixed resonances, as realized by excitation with the circularly polarized laser, is shown in Fig. 11 (c). Here, the emission direction oscillates, which results from the beating between the two resonances as explained above for the oscillating populations. Again, the negative z direction is avoided. The same behavior can be found for excitations with elliptically polarized light, which is not shown here.

The impact of the Coulomb barrier in the left dot, which hinders the ICD electron in moving into the negative z direction, was also observed in [A.3] for a geometrical study, where the ICD rate for the decay of either resonance was determined in dependence of the inter-QD distance. It was found that for the pure decay of the x- and z-resonance the ICD rate oscillates about R^{-6} with mean deviations of 30% and 24%. Those oscillations have been observed earlier for the QDs-in-a-wire scenario with deviations of 85% on average,[53] where they came from the reflection of the ICD electron at the left QD Coulomb barrier followed by a recapture. The oscillations for the dots with two-dimensional continuum are however smaller, which means the chance for recapture is diminished.

In conclusion, the QD-ICD is a highly-efficient decay process either inside a one-dimensional nanowire or on a two-dimensional wetting layer, where ICD is faster for the latter system in which the ICD electron can move along two directions. For the initiation of ICD in negatively charged QDs weak infrared laser pulses with a focus on the eventually energy emitting dot are best suited. Moreover, the polarization of the resonantly exciting laser controls the mixture of resonance states that forms the decaying state, which itself has an impact on the electron emission direction. Going beyond the formerly investigated QDs in a wire, a more easily accessible quantum dot system was proposed here in terms of laterally arranged quantum dots on a two-dimensional surface, which are commonly realized through self-assembly or lithographically. Those structures are more widespreadly investigated. Hence, they are promising for detecting ICD inside QDs in a future experiment, as well as for a possible device application e.g. for improved QD infrared photodetectors that function by means of ICD.

It is for sure that the QD-ICD has a lot more features than what can possibly be explained by the simplified model of this thesis. There is an indescribable amount of theory waiting and many device applications could profit from this. For example, in a more concrete experimental setup the system might consist of a cluster of more than two QDs with as many electrons. This would make the study of a cascade of ICD processes interesting, but would also require the computation of a high-dimensional problem. QD-ICD could also be a prominent process to be used for sensitized solar cells.[116],[117] Respective QDs are neutral and have a band gap in the range of 1 eV such that excitations by visible or near-IR light lead to inter-band transitions, thus to the formation of excitons. QD-ICD in combination with exciton Rabi oscillations can be also interesting for quantum information processing.[96],[118],[119] Another promising type of system are colloidal QDs, since they are relatively straightforward to produce in solution with a possibility to control the inter-dot distance.[93],[120] To study ICD in these types of dots would require to incorporate a third continuum dimension.

References

[1] M. Thompson, M. D. Baker, A. Christie, and J. F. Tyson. *Auger Electron Spectroscopy.* Wiley, New York, 1985.

[2] L. V. Azaroff. *X-Ray Spectroscopy.* McGraw-Hill, New York, 1974.

[3] T. Förster. Zwischenmolekulare Energiewanderung und Fluoreszenz. *Ann. Phys.*, **437**:55–75, 1948.

[4] T. W. J. Gadella. *FRET and FLIM Techniques.* Elsevier Science, Amsterdam, 2009.

[5] G. D. Scholes and D. L. Andrews. Resonance energy transfer and quantum dots. *Phys. Rev. B*, **72**:125331, 2005.

[6] L. S. Cederbaum, J. Zobeley, and F. Tarantelli. Giant intermolecular decay and fragmentation of clusters. *Phys. Rev. Lett.*, **79**:4778–4781, 1997.

[7] J. Zobeley, L. S. Cederbaum, and F. Tarantelli. Intermolecular Coulombic decay of molecular clusters: Identification of the decay mechanism using a new hole-population analysis. *J. Phys. Chem. A*, **103**:11145–11160, 1999.

[8] K. Kreidi, T. Jahnke, Th. Weber, T. Havermeier, X. Liu, Y. Morisita, S. Schössler, L.Ph.H. Schmidt, M. Schöffler, M. Odenweller, N. Neumann, L. Foucar, J. Titze, B. Ulrich, F. Sturm, C. Stuck, R. Wallauer, S. Voss, I. Lauter, H. K. Kim, M. Rudloff, H. Fukuzawa, G. Prümper, N. Saito, K. Ueda, A. Czasch, O. Jagutzki, H. Schmidt-Böcking, Stoychev S., Ph. V. Demekhin, and R. Dörner. Relaxation processes following 1s photoionization and Auger decay in Ne_2. *Phys. Rev. A*, **78**:043422, 2008.

[9] T. Jahnke, A. Czasch, M. S. Schöffler, S. Schössler, A. Knapp, M. Käsz, J. Titze, C. Wimmer, K. Kreidi, R. E. Grisenti, A. Staudte, O. Jagutzki, U. Hergenhahn, H. Schmidt-Böcking, and R. Dörner. Experimental observation of interatomic Coulombic decay in neon dimers. *Phys. Rev. Lett.*, **93**:163401, 2004.

[10] U. Hergenhahn. Interatomic and intermolecular Coulombic decay: The early years. *J. Electron Spectrosc. Relat. Phenom.*, **184**:78, 2011.

[11] R. Santra and L. S. Cederbaum. Non-Hermitian electronic theory and applications to clusters. *Phys. Rep.*, **368**:1–117, 2002.

[12] V. Averbukh, Ph.V. Demekhin, P. Kolorenč, S. Scheit, S.D. Stoychev, A.I. Kuleff, Y.-C. Chiang, K. Gokhberg, S. Kopelke, N. Sisourat, and L.S. Cederbaum. Interatomic electronic decay processes in singly and multiply ionized clusters. *J. Electron Spectrosc. Relat. Phenom.*, **183**:36–47, 2011.

[13] T. Jahnke. Interatomic and intermolecular Coulombic decay: The coming of age story. *J. Phys. B: At. Mol. Opt. Phys.*, **48**:082001, 2015.

[14] V. Averbukh, I. B. Müller, and L. S. Cederbaum. Mechanism of interatomic Coulombic decay in clusters. *Phys. Rev. Lett.*, **93**:263002, 2004.

[15] R. Santra, J. Zobeley, and L. S. Cederbaum. Electronic decay of valence holes in clusters and condensed matter. *Phys. Rev. B*, **64**:245104, 2001.

[16] T. Jahnke, A. Czasch, M. Schöffler, S. Schössler, M. Käsz, J. Titze, K. Kreidi, R. E. Grisenti, A. Staudte, O. Jagutzki, L. Ph. H. Schmidt, Th. Weber, H. Schmidt-Böcking, K. Ueda, and R. Dörner. Experimental separation of virtual photon exchange and electron transfer in interatomic Coulombic decay of neon dimers. *Phys. Rev. Lett.*, **99**:153401, 2007.

[17] S. Barth, S. Joshi, S. Marburger, V. Ulrich, A. Lindblad, G. Öhrwall, O. Björneholm, and U. Hergenhahn. Observation of resonant interatomic Coulombic decay in Ne clusters. *J. Chem. Phys.*, **122**:241102, 2005.

[18] T. Aoto, K. Ito, Y. Hikosaka, E. Shigemasa, F. Penent, and P. Lablanquie. Properties of resonant interatomic Coulombic decay in Ne dimers. *Phys. Rev. Lett.*, **97**:243401, 2006.

[19] K. Gokhberg, A. B. Trofimov, T. Sommerfeld, and L. S. Cederbaum. Ionization of metal atoms following valence-excitation of neighbouring molecules. *Europhys. Lett.*, **72**:228, 2005.

[20] K. Gokhberg, V. Averbukh, and L. S. Cederbaum. Interatomic decay of inner-valence-excited states in clusters. *J. Chem. Phys.*, **124**:144315, 2006.

[21] L. S. Cederbaum. Ultrafast intermolecular energy transfer from vibrations to electronic motion. *Phys. Rev. Lett.*, **121**:223001, 2018.

[22] J. Zobeley, L. S. Cederbaum, and F. Tarantelli. Highly excited electronic states of molecular clusters and their decay. *J. Chem. Phys.*, **108**:9737–9750, 1998.

[23] R. Santra, L.S. Cederbaum, and H.-D. Meyer. Electronic decay of molecular clusters: Non-stationary states computed by standard quantum chemistry methods. *Chem. Phys. Lett.*, **303**:413 – 419, 1999.

[24] R. Santra, J. Zobeley, L. S. Cederbaum, and N. Moiseyev. Interatomic Coulombic decay in van der Waals clusters and impact of nuclear motion. *Phys. Rev. Lett.*, **85**:4490–4493, 2000.

[25] N. Moiseyev, R. Santra, J. Zobeley, and L. S. Cederbaum. Fingerprints of the nodal structure of autoionizing vibrational wave functions in clusters: Interatomic Coulombic decay in Ne dimer. *J. Chem. Phys.*, **114**:7351–7360, 2001.

[26] S. Scheit, L. S. Cederbaum, and H.-D. Meyer. Time-dependent interplay between electron emission and fragmentation in the interatomic Coulombic decay. *J. Chem. Phys.*, **118**:2092–2107, 2003.

[27] S. Marburger, O. Kugeler, U. Hergenhahn, and T. Möller. Experimental evidence for interatomic Coulombic decay in Ne clusters. *Phys. Rev. Lett.*, **90**:203401, 2003.

[28] G. Öhrwall, M. Tchaplyguine, M. Lundwall, R. Feifel, H. Bergersen, T. Rander, A. Lindblad, J. Schulz, S. Peredkov, S. Barth, S. Marburger, U. Hergenhahn, S. Svensson, and O. Björneholm. Femtosecond interatomic Coulombic decay in free neon clusters: Large lifetime differences between surface and bulk. *Phys. Rev. Lett.*, **93**:173401, 2004.

[29] S. Kopelke, K. Gokhberg, V. Averbukh, F. Tarantelli, and L. S. Cederbaum. Ab initio interatomic decay widths of excited states by applying Stieltjes imaging to Lanczos pseudospectra. *J. Chem. Phys.*, **134**:094107, 2011.

[30] T. Ouchi, K. Sakai, H. Fukuzawa, X.-J. Liu, I. Higuchi, Y. Tamenori, K. Nagaya, H. Iwayama, M. Yao, D. Zhang, D. Ding, A. I. Kuleff, S. D. Stoychev, Ph. V. Demekhin, N. Saito, and K. Ueda. Three-electron interatomic Coulombic decay from the inner-valence double-vacancy states in NeAr. *Phys. Rev. Lett.*, **107**:053401, 2011.

[31] R. Santra and L. S. Cederbaum. Coulombic energy transfer and triple ionization in clusters. *Phys. Rev. Lett.*, **90**:153401, 2003.

[32] Y. Morishita, X.-J. Liu, N. Saito, T. Lischke, M. Kato, G. Prümper, M. Oura, H. Yamaoka, Y. Tamenori, I. H. Suzuki, and K. Ueda. Experimental evidence of interatomic Coulombic decay from the Auger final states in argon dimers. *Phys. Rev. Lett.*, **96**:243402, 2006.

[33] S. D. Stoychev, A. I. Kuleff, F. Tarantelli, and L. S. Cederbaum. On the interatomic electronic processes following Auger decay in neon dimer. *J. Chem. Phys.*, **129**:074307, 2008.

[34] E. F. Aziz, N. Ottosson, M. Faubel, I. V. Hertel, and B. Winter. Interaction between liquid water and hydroxide revealed by core-hole de-excitation. *Nature*, **455**:89, 2008.

[35] W. Pokapanich, H. Bergersen, I. L. Bradeanu, R.R.T. Marinho, A. Lindblad, S. Legendre, A. Rosso, S. Svensson, O. Björneholm, M. Tchaplyguine, G. Öhrwall, N. V. Kryzhevoi, and L. S. Cederbaum. Auger electron spectroscopy as a probe of the solution of aqueous ions. *J. Am. Chem. Soc.*, **131**:7264, 2009.

[36] M. Mucke, M. Braune, S. Barth, M. Förstel, T. Lischke, V. Ulrich, T. Arion, U. Becker, A Bradshaw, and U. Hergenhahn. A hitherto unrecognized source of low-energy electrons in water. *Nat. Phys.*, **6**:143, 2010.

[37] T. Jahnke, H. Sann, T. Havermeier, K. Kreidi, C. Stuck, M. Meckel, M. Schöffler, N. Neumann, R. Wallauer, S. Voss, A. Czasch, O. Jagutzki, A. Malakzadeh, F. Afaneh, Th. Weber, H. Schmidt-Böcking, and R. Dörner. Ultrafast energy transfer between water molecules. *Nat. Phys.*, **6**:139, 2010.

[38] K. Gokhberg and L. S. Cederbaum. Environment assisted electron capture. *J. Phys. B: At. Mol. Opt. Phys.*, **42**:231001, 2009.

[39] K. Gokhberg and L. S. Cederbaum. Interatomic Coulombic electron capture. *Phys. Rev. A*, **82**:052707, 2010.

[40] F. M. Pont, A. Bande, and L. S. Cederbaum. Controlled energy-selected electron capture and release in double quantum dots. *Phys. Rev. B*, **88**:241304, 2013.

[41] A. Molle, E. R. Berikaa, F. M. Pont, and A. Bande. Quantum size effect affecting environment assisted electron capture in quantum confinements. *J. Chem. Phys.*, **150**:224105, 2019.

[42] J. Titze, M. S. Schöffler, H.-K. Kim, F. Trinter, M. Waitz, J. Voigtsberger, N. Neumann, B. Ulrich, K. Kreidi, R. Wallauer, M. Odenweller, T. Havermeier, S. Schössler, M. Meckel, L. Foucar, T. Jahnke, A. Czasch, L. Ph. H. Schmidt, O. Jagutzki, R. E. Grisenti, H. Schmidt-Böcking, H. J. Lüdde, and R. Dörner. Ionization dynamics of helium dimers in fast collisions with He^{++}. *Phys. Rev. Lett.*, **106**:033201, 2011.

[43] H. K. Kim, H. Gassert, M. S. Schöffler, J. N. Titze, M. Waitz, J. Voigtsberger, F. Trinter, J. Becht, A. Kalinin, N. Neumann, C. Zhou, L.Ph.H. Schmidt, O. Jagutzki, A. Czasch, H. Merabet, H. Schmidt-Böcking, T. Jahnke, A. Cassimi, and R. Dörner. Ion-impact-induced interatomic Coulombic decay in neon and argon dimers. *Phys. Rev. A*, **88**:042707, 2013.

[44] S. Yan, P. Zhang, X. Ma, S. Xu, B. Li, X. L. Zhu, W. T. Feng, S. F. Zhang, D. M. Zhao, R. Zhang, D. Guo, and H. P. Liu. Observation of interatomic Coulombic decay and electron-transfer-mediated decay in high-energy electron-impact ionization of Ar_2. *Phys. Rev. A*, **88**:042712, 2013.

[45] S. Yan, P. Zhang, X. Ma, S. Xu, S. X. Tian, B. Li, X. L. Zhu, W. T. Feng, and D. M. Zhao. Dissociation mechanisms of the Ar trimer induced by a third atom in high-energy electron-impact ionization. *Phys. Rev. A*, **89**:062707, 2014.

[46] P. H. P. Harbach, M. Schneider, S. Faraji, and A. Dreuw. Intermolecular Coulombic decay in biology: The initial electron detachment from $FADH^-$ in DNA photolyases. *J. Phys. Chem. Lett.*, **4**:943–949, 2013.

[47] A. Dreuw and S. Faraji. A quantum chemical perspective on (6-4) photolesion repair by photolyases. *Phys. Chem. Chem. Phys.*, **15**:19957–19969, 2013.

[48] A. I. Ekimov and A. A. Onushchenko. Quantum size effect in three-dimensional microscopic semiconductor crystals. *JETP Lett.*, **34**:345, 1981.

[49] A. L. Efros. Interband absorption of light in a semiconductor sphere. *Sov. Phys. Semicond.*, **16**:772–775, 1982.

[50] L. E. Brus. A simple model for the ionization potential, electron affinity, and aqueous redox potentials of small semiconductor crystallites. *J. Chem. Phys.*, **79**:5566–5571, 1983.

[51] M. A. Reed, R. T. Bate, K. Bradshaw, W. M. Duncan, W. R. Frensley, J. W. Lee, and H. D. Shih. Spatial quantization in GaAs-AlGaAs multiple quantum dots. *J. Vac. Sci. Technol. B*, **4**:358–360, 1986.

[52] I. Cherkes and N. Moiseyev. Electron relaxation in quantum dots by the interatomic Coulombic decay mechanism. *Phys. Rev. B*, **83**:113303, 2011.

[53] A. Bande, K. Gokhberg, and L. S. Cederbaum. Dynamics of interatomic Coulombic decay in quantum dots. *J. Chem. Phys.*, **135**:144112, 2011.

[54] A. Bande. Electron dynamics of interatomic Coulombic decay in quantum dots induced by a laser field. *J. Chem. Phys.*, **138**:214104, 2013.

[55] M. A. Kastner. Artificial atoms. *Phys. Today*, **46**:24–31, 1993.

[56] U. Bockelmann. Exciton relaxation and radiative recombination in semiconductor quantum dots. *Phys. Rev. B*, **48**:17637–17640, 1993.

[57] U. Bockelmann and T. Egeler. Electron relaxation in quantum dots by means of Auger processes. *Phys. Rev. B*, **46**:15574–15577, 1992.

[58] Al. L. Efros and M. Rosen. Random telegraph signal in the photoluminescence intensity of a single quantum dot. *Phys. Rev. Lett.*, **78**:1110–1113, 1997.

[59] V. I. Klimov, A. A. Mikhailovsky, S. Xu, A. Malko, J. A. Hollingsworth, C. A. Leatherdale, H.-J. Eisler, and M. G. Bawendi. Optical gain and stimulated emission in nanocrystal quantum dots. *Science*, **290**:314–317, 2000.

[60] A. Kurzmann, A. Ludwig, A. D. Wieck, A. Lorke, and M. Geller. Auger recombination in self-assembled quantum dots: Quenching and broadening of the charged exciton transition. *Nano Lett.*, **16**:3367–3372, 2016.

[61] A. Bande, F. M. Pont, P. Dolbundalchok, K. Gokhberg, and L. S. Cederbaum. Electron dynamics of interatomic Coulombic decay in quantum dots: Singlet initial state. *EPJ Web Conf.*, **41**:04031, 2013.

[62] P. Dolbundalchok, D. Peláez, E. F. Aziz, and A. Bande. Geometrical control of the interatomic Coulombic decay process in quantum dots for infrared photodetectors. *J. Comput. Chem.*, **37**:2249–2259, 2016.

[63] P. Lodahl, A. F. van Driel, I. S. Nikolaev, A. Irman, K. Overgaag, D. Vanmaekelbergh, and W. L. Vos. Controlling the dynamics of spontaneous emission from quantum dots by photonic crystals. *Nature*, **430**:654–657, 2004.

[64] A. Bande. Acoustic phonon impact on the inter-Coulombic decay process in charged quantum dot pairs. *Mol. Phys.*, 2019. **DOI:** 10.1080/00268976.2019.1574986.

[65] F. Weber, E. F. Aziz, and A. Bande. Interdependence of ICD rates in paired quantum dots on geometry. *J. Comput. Chem.*, **38**:2141–2150, 2017.

[66] H.-D. Meyer, U. Manthe, and L. S. Cederbaum. The multi-configurational time-dependent Hartree approach. *Chem. Phys. Lett.*, **165**:73–78, 1990.

[67] U. Manthe, H.-D. Meyer, and L. S. Cederbaum. Wave-packet dynamics within the multiconfiguration Hartree framework: General aspects and application to NOCl. *J. Chem. Phys.*, **97**:3199–3213, 1992.

[68] U. Fano. Effects of configuration interaction on intensities and phase shifts. *Phys. Rev.*, **124**:1866–1878, 1961.

[69] S.-W. Lee, K. Hirakawa, and Y. Shimada. Bound-to-continuum intersubband photoconductivity of self-assembled InAs quantum dots in modulation-doped heterostructures. *Appl. Phys. Lett.*, **75**:1428–1430, 1999.

[70] I. I. Rabi. Space quantization in a gyrating magnetic field. *Phys. Rev.*, **51**:652–654, 1937.

[71] I. I. Rabi, S. Millman, P. Kusch, and J. R. Zacharias. The molecular beam resonance method for measuring nuclear magnetic moments. the magnetic moments of $_3\mathrm{Li}^6$, $_3\mathrm{Li}^7$ and $_9\mathrm{F}^{19}$. *Phys. Rev.*, **55**:526–535, 1939.

[72] A. Zrenner. A close look on single quantum dots. *J. Chem. Phys.*, **112**:7790–7798, 2000.

[73] M. G. Bawendi, P. J. Carroll, William L. Wilson, and L. E. Brus. Luminescence properties of CdSe quantum crystallites: Resonance between interior and surface localized states. *J. Chem. Phys.*, **96**:946–954, 1992.

[74] H. Drexler, D. Leonard, W. Hansen, J. P. Kotthaus, and P. M. Petroff. Spectroscopy of quantum levels in charge-tunable InGaAs quantum dots. *Phys. Rev. Lett.*, **73**:2252–2255, 1994.

[75] S. Sauvage, P. Boucaud, F. H. Julien, J.-M. Gérard, and V. Thierry-Mieg. Intraband absorption in n-doped InAs/GaAs quantum dots. *Appl. Phys. Lett.*, **71**:2785–2787, 1997.

[76] P. Guyot-Sionnest and M. A. Hines. Intraband transitions in semiconductor nanocrystals. *Appl. Phys. Lett.*, **72**:686–688, 1998.

[77] N. N. Ledentsov. Quantum dot laser. *Semicond. Sci. Technol.*, **26**:014001, 2011.

[78] P. Michler, A. Kiraz, C. Becher, W. V. Schoenfeld, P. M. Petroff, L. Zhang, E. Hu, and A. Imamoglu. A quantum dot single-photon turnstile device. *Science*, **290**:2282–2285, 2000.

[79] S. Maimon, E. Finkman, G. Bahir, S. E. Schacham, J. M. Garcia, and P. M. Petroff. Intersublevel transitions in InAs/GaAs quantum dots infrared photodetectors. *Appl. Phys. Lett.*, **73**:2003–2005, 1998.

[80] D. Pan, E. Towe, and S. Kennerly. Normal-incidence intersubband (In, Ga)As/GaAs quantum dot infrared photodetectors. *Appl. Phys. Lett.*, **73**:1937–1939, 1998.

[81] H. C. Liu, M. Gao, J. McCaffrey, Z. R. Wasilewski, and S. Fafard. Quantum dot infrared photodetectors. *Appl. Phys. Lett.*, **78**:79–81, 2001.

[82] S.-F. Tang, S.-Y. Lin, and S.-C. Lee. Near-room-temperature operation of an InAs/GaAs quantum-dot infrared photodetector. *Appl. Phys. Lett.*, **78**:2428–2430, 2001.

[83] P. Harrison and A. Valavanis. *Quantum Wells, Wires and Dots.* John Wiley & Sons, Ltd., Chichester, 2016.

[84] H. Bruus and K. Flensberg. *Many-Body Quantum Theory in Condensed Matter Physics: An Introduction.* Oxford University Press, Oxford, 2004.

[85] H. Ibach and H. Lüth. *Festkörperphysik: Einführung in die Grundlagen.* Springer, Berlin Heidelberg, 2013.

[86] L. de Broglie. Waves and quanta. *Nature*, **112**:540, 1923.

[87] P. M. Petroff, A. Lorke, and A. Imamoglu. Epitaxially self-assembled quantum dots. *Phys. Today*, **54**:46–52, 2001.

[88] L. Wang, A. Rastelli, S. Kiravittaya, M. Benyoucef, and O. G. Schmidt. Self-assembled quantum dot molecules. *Adv. Mater.*, **21**:2601–2618, 2009.

[89] E. Zallo, P. Atkinson, L. Wang, A. Rastelli, and O. G. Schmidt. Epitaxial growth of lateral quantum dot molecules. *Phys. Status Solidi B*, **249**:702–709, 2012.

[90] D. Bimberg, M. Grundmann, and N. N. Ledentsov. *Quantum Dot Heterostructures.* John Wiley & Sons, Ltd., Chichester, 1999.

[91] L. P. Kouwenhoven, C. M. Marcus, P. L. McEuen, S. Tarucha, R. M. Westervelt, and N. S. Wingreen. *Mesoscopic Electron Transport.* Kluwer Academic, Dordrecht, 1997.

[92] W. G. van der Wiel, S. De Franceschi, J. M. Elzerman, T. Fujisawa, S. Tarucha, and L. P. Kouwenhoven. Electron transport through double quantum dots. *Rev. Mod. Phys.*, **75**:1–22, 2002.

[93] Y. Yin and A. P. Alivisatos. Colloidal nanocrystal synthesis and the organic-inorganic interface. *Nature*, **437**:664–670, 2005.

[94] S. Bednarek, B. Szafran, T. Chwiej, and J. Adamowski. Effective interaction for charge carriers confined in quasi-one-dimensional nanostructures. *Phys. Rev. B*, **68**:045328, 2003.

[95] D. J. Tannor. *Introduction to Quantum Mechanics*. University Science Books, USA, 2007.

[96] J. Luo, W. Lai, D. Lu, C. Du, Y. Liu, S. Gong, D. Shi, and C. Guo. Pronounced enhancement of exciton rabi oscillation for a two-photon transition based on quantum dot coupling control. *J. Phys. B: At. Mol. Opt. Phys.*, **45**:035402, 2012.

[97] R. Kosloff and D. Kosloff. Absorbing boundaries for wave propagation problems. *J. Comput. Phys.*, **63**:363–376, 1986.

[98] D. Neuhauser and M. Baer. The time-dependent Schrödinger equation: Application of absorbing boundary conditions. *J. Chem. Phys.*, **90**:4351–4355, 1989.

[99] U. V. Riss and H.-D. Meyer. Calculation of resonance energies and widths using the complex absorbing potential method. *J. Phys. B: At. Mol. Opt. Phys.*, **26**:4503–4535, 1993.

[100] U. V. Riss and H.-D. Meyer. Investigation on the reflection and transmission properties of complex absorbing potentials. *J. Chem. Phys.*, **105**:1409–1419, 1996.

[101] Y. Sajeev and N. Moiseyev. Theory of autoionization and photoionization in two-electron spherical quantum dots. *Phys. Rev. B*, **78**:075316, 2008.

[102] NSM Archive - Physical properties of semiconductors. http://matprop.ru/GaAs_basic (accessed 21-Nov-2018).

[103] P. A. M. Dirac. Note on exchange phenomena in the Thomas atom. *Math. Proc. Cambridge*, **26**:376–385, 1930.

[104] J. Frenkel. *Wave Mechanics*. Clarendon Press, Oxford, 1934.

[105] A.D. McLachlan. A variational solution of the time-dependent Schrödinger equation. *Mol. Phys.*, **8**:39–44, 1964.

[106] M. Beck. The multiconfiguration time-dependent Hartree (MCTDH) method: A highly efficient algorithm for propagating wavepackets. *Phys. Rep.*, **324**:1–105, 2000.

[107] H.-D. Meyer, F. Gatti, and G. A. Worth. *Multidimensional Quantum Dynamics - MCTDH Theory and Applications*. Wiley-VCH, Weinheim, 2009.

[108] J. C. Light, I. P. Hamilton, and J. V. Lill. Generalized discrete variable approximation in quantum mechanics. *J. Chem. Phys.*, **82**:1400–1409, 1985.

[109] J. C. Light. *Discrete variable representations in quantum dynamics* in Time-Dependent Quantum Molecular Dynamics, pages 185–199. Springer US, New York, 1992.

[110] J. C. Light and T. Carrington Jr. *Discrete Variable Representations and their Utilization* in Advances in Chemical Physics, pages 263–310. Wiley-Blackwell, 2007.

[111] D. Peláez and H.-D. Meyer. The multigrid POTFIT (MGPF) method: Grid representations of potentials for quantum dynamics of large systems. *J. Chem. Phys.*, **138**:014108, 2013.

[112] R. Kosloff and H. Tal-Ezer. A direct relaxation method for calculating eigenfunctions and eigenvalues of the Schrödinger equation on a grid. *Chem. Phys. Lett.*, **127**:223–230, 1986.

[113] C. Leforestier and R. E. Wyatt. Optical potential for laser induced dissociation. *J. Chem. Phys.*, **78**:2334–2344, 1983.

[114] Y.-C. Chiang, Ph. V. Demekhin, A. I. Kuleff, S. Scheit, and L. S. Cederbaum. Linewidth and lifetime of atomic levels and the time evolution of spectra and coincidence spectra. *Phys. Rev. A*, **81**:032511, 2010.

[115] Ph. V. Demekhin and L. S. Cederbaum. Strong interference effects in the resonant Auger decay of atoms induced by intense x-ray fields. *Phys. Rev. A*, **83**:023422, 2011.

[116] A.J Nozik. Quantum dot solar cells. *Physica E*, **14**:115–120, 2002.

[117] P. V. Kamat. Quantum dot solar cells. Semiconductor nanocrystals as light harvesters. *J. Phys. Chem. C*, **112**:18737–18753, 2008.

[118] T. H. Stievater, Xiaoqin Li, D. G. Steel, D. Gammon, D. S. Katzer, D. Park, C. Piermarocchi, and L. J. Sham. Rabi oscillations of excitons in single quantum dots. *Phys. Rev. Lett.*, **87**:133603, 2001.

[119] G. Ya. Slepyan, A. Magyarov, S. A. Maksimenko, A. Hoffmann, and D. Bimberg. Rabi oscillations in a semiconductor quantum dot: Influence of local fields. *Phys. Rev. B*, **70**:045320, 2004.

[120] P. Alivisatos. Colloidal quantum dots. From scaling laws to biological applications. *Pure Appl. Chem.*, **72**:3–9, 2000.

A Publications

In this chapter the scientific publications [A.1]-[A.3] composing this thesis are presented in chronological order. For each publication the contributions by the individual authors are outlined.

A.1 Strong field control of the interatomic Coulombic decay process in quantum dots

Anika Haller, Ying-Chih Chiang, Maximilian Menger, Emad F. Aziz and Annika Bande

Chem. Phys. 482, 135-145 (2017)

DOI: 10.1016/j.chemphys.2016.09.020

URL: https://doi.org/10.1016/j.chemphys.2016.09.020

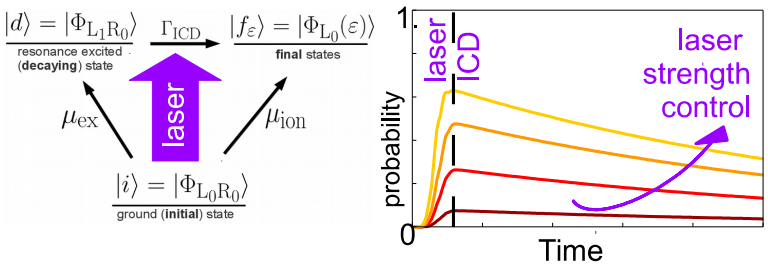

Figure A.1: Graphical abstract. Reprint with permission from Haller et al. [A.1] (©2017 Elsevier)

Author contributions: The conception of this work was conceived by AB. Preliminary calculations were conducted by MM during his Bachelor thesis with AB in 2013. **AH** performed all calculations, data analysis and visual presentation of the results. YCC derived the analytical expressions for the state resolved equations of motions and wrote a Fortran program for numerical solution. The theory section was written by **AH**. The introduction and the conclusion were written by AB. AB and **AH** analyzed and discussed the results in detail and composed the results section of this article. All authors contributed to bring the pre-final version of the manuscript into a submittable form.

A.2 Favoritism of quantum dot inter-Coulombic decay over direct and multi-photon ionization by laser strength and focus

Anika Haller and Annika Bande

J. Chem. Phys. 149, 134102 (2018)

DOI: 10.1063/1.5042208

URL: https://doi.org/10.1063/1.5042208

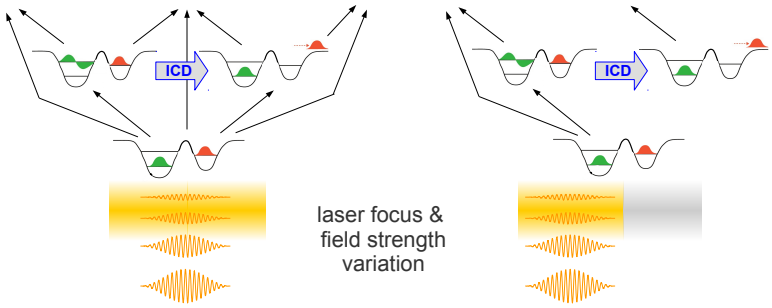

Figure A.2: Graphical abstract created exclusively for this thesis. Figure adapted from [A.2].

Author contributions: The conception of this work was conceived by AB. **AH** performed all calculations, data analysis and visual presentation of the results. The manuscript was mostly written by **AH** with considerable input from AB.

A.3 Inter-Coulombic decay in laterally arranged quantum dots controlled by polarized lasers

Anika Haller, Daniel Peláez and Annika Bande

J. Phys. Chem. C 123, 14754-14765 (2019)

DOI: 10.1021/acs.jpcc.9b01250

URL: https://doi.org/10.1021/acs.jpcc.9b01250

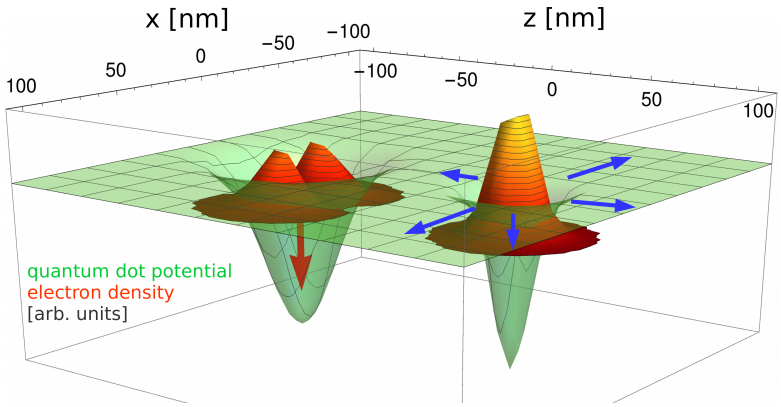

Figure A.3: Graphical abstract. Reprint with permission from Haller et al. [A.3] (©2019 American Chemical Society)

Author contributions: The conception of this work was conceived by AB. DP provided the Coulomb potential files (natpot) that he calculated with the Multigrid POTFIT program (MGPF) that was developed by him earlier with another co-author. **AH** performed all electron dynamics calculations, data analysis and visual presentation of the results. AB wrote the introduction and the conclusions, **AH** the theory section except for the MGPF part that was written by DP. The results section was written by **AH**. All authors contributed to the final version of the manuscript by multiple iterations.